

# X-ray reprocessing: Through the eclipse spectra of low mass X-ray binaries with *XMM-Newton*

Nafisa Aftab<sup>a,\*</sup>, Biswajit Paul<sup>a</sup>

<sup>a</sup>*Raman Research Institute, C V Raman Avenue, Sadashivanagar, Bangalore 560080, India*

---

## Abstract

Eclipsing X-ray binaries make an ideal condition to study reprocessed X-rays, as the X-rays detected during eclipse are purely reprocessed while the much brighter primary X-rays are blocked by the companion star. We carried out a comprehensive study of X-ray reprocessing with four eclipsing Low Mass X-ray Binary (LMXB) systems by comparing X-ray spectra during and outside eclipse with *XMM-Newton* EPIC pn observations. The 17 observations of MXB 1659–298, AX J1745.6–2901, EXO 0748–676 and XTE J1710–281 give unique features of the systems. For example, X-ray reprocessing characteristics in AX J1745.6–2901 is found to be nearly same irrespective of the intensity state; there is an indication of different types of variable warp structures in the inner accretion disk in EXO 0748–676, a high out-of-eclipse to eclipse flux ratio in XTE J1710–281 inspite of a large size of the accretion disk perhaps indicates low scale height of the accretion disk. The eclipse spectra for some of the LMXB sources are reported for the first time. We have derived the fractional visible area of the accretion disk during maximum eclipse phase for various obscuration geometries. The out-of-eclipse to eclipse flux ratio in LMXBs observed to be smaller compared to that found in High Mass X-ray Binaries. This indicates greater reprocessing in LMXBs despite having less dense, less extended stellar wind from the companion. The X-ray reprocessing efficiencies observed in LMXBs indicate large dependencies of X-ray reprocessing on the scale height of the accretion disk, relative size of the disk compared to the companion and some other unknown factors.

*Keywords:*

(stars:) binaries: eclipsing, stars: neutron, stars: low-mass

---

## 1. Introduction

In X-ray binaries, most of the X-rays originate in the inner accretion disk (in case of disk accretion) and boundary layer of the neutron star and from the pole of the neutron star in case of pulsars. These X-rays are called primary X-rays. Some of these X-rays come out directly. A significant fraction of the primary X-rays interacts with the surrounding matter and are re-emitted in different directions. This phenomenon is known as X-ray reprocessing and the re-emitted X-rays are called reprocessed X-rays. Depending upon the type of interaction, the reprocessed or

---

\*Corresponding Author

Email address: [aftabnafisa@gmail.com](mailto:aftabnafisa@gmail.com) (Nafisa Aftab)

secondary emission could be X-ray, UV and / or optical (Aftab, Paul and Kretschmar, 2019). Reprocessing of X-rays have been observed in active galactic nuclei (AGN), accreting systems with black hole, neutron star, white dwarf as compact objects (Zycki et al. 1994, Gierliński et al. 2009, de Jong et al. 1996, Suleimanov et al. 2003).

In this work we focus on X-ray reprocessing characteristics of Low Mass X-ray Binary (LMXB) systems. In LMXBs the companion star has a mass  $M \leq M_{\odot}$  as donor star and either black hole or neutron star as compact object. The companion is often a late type star (spectral type A or later i.e K, L, M types) or a white dwarf in a few cases. In LMXB systems the main reprocessing agent is the accretion disk and any structure on the disk if present. The observability X-ray reprocessing characteristics in LMXBs depend upon several factors, for example i) the scale height of the accretion disk ii) inclination of the system with respect to our line of sight iii) the size of the accretion disk with respect to the size of the companion iv) structures on the accretion disk v) distribution of matter in the system and their densities vi) the chemical composition and ionization levels of the matter around the compact object vii) wind outflow from the accretion disk or accretion disk atmosphere viii) orbital phase of the system. The scale height of the accretion disk determines the solid angle covered by the accretion disk surface to central source, hence how much central radiation will be reprocessed. The inclination determines how much fraction of the central radiation will be scattered towards us.

Study of X-ray reprocessing gives us an understanding of the environment that causes the reprocessing of X-rays. But the main challenge in this study is that, the detected X-rays are a mixture of primary and reprocessed X-rays and the primary X-rays are much brighter than the reprocessed X-rays. However during eclipse, the primary X-rays from the compact object are completely blocked by the companion and the received X-rays are the reprocessed X-rays only, which is free of primary emission. Hence X-rays received during eclipses from the eclipsing LMXBs are ideal to study the X-ray reprocessing in these systems. The portion of the accretion disk visible to us during eclipse depends upon the relative size of the disk compared to the size of the companion, inclination of the system with respect to the line of sight and the orbital separation.

In this work we have analyzed four LMXB systems (MXB 1659–298, EXO 0748–676, AX J1745.6–2901 and XTE 1710–281) during eclipse and out-of-eclipse phases with *XMM-Newton* EPIC pn. The transient, bursting and dipping neutron star LMXB system MXB 1659–298 was discovered with *SAS-3* (Lewin et al., 1976). The source is an eclipsing system (Cominsky et al., 1984) with an orbital period of 7.116 hr (Cominsky et al., 1989). Jain et al. (2017) suggests a massive third body around the binary orbit with mid eclipse time analysis of the source with *RXTE* and *XMM-Newton*. EXO 0748–676, a neutron star LMXB system was discovered with *EXOSAT* in 1985 and was found to have an orbital period of 3.824 hour and eclipses lasting for 8.3 min (Parmar et al., 1985). After 24 years of continuous accretion, the source went into quiescence in 2008 (Trigo et al., 2011). Raman et al. (2017) have inferred a strong evidence of accretion disk evolution at time scale of few hours, from the modulation of optical lightcurve of the same *XMM-Newton* observations we have analyzed in this work. AX J1745.6–2901 is an eclipsing neutron star LMXB system 1.45 arcmin from Sgr A\*, was discovered by ASCA during 1993-1994 outburst with an orbital period of  $\sim 8.356$  hours (Maeda et al., 1996). *XMM-Newton* and *Chandra* data showed evidence of different dust layers surrounding the source (Jin et al., 2017, 2018), which causes asymmetric shape of the lightcurves during eclipses. XTE J1710–281 is a transient LMXB system (Markwardt et al., 1998) serendipitously detected with *RXTE-PCA*. The source shows eclipse for an average duration of  $\sim 420$  s in each orbit with an orbital period of 3.281 hr (Jain and Paul, 2011). Raman et al. (2018) have found a signature of accretion disk

winds in this source through the observation of highly ionized Fe lines with *Suzaku*, they have also observed evolution of dips in each orbit with *Chandra* data.

Eclipse spectrum of some of the sources have been studied before (MXB 1659–298: Sidoli et al. 2001, EXO 0748–676: Psaradaki et al. 2018) but here we report results from first comprehensive study of LMXB eclipse and out-of-eclipse spectra with *XMM-Newton* EPIC pn. A similar investigation of the X-ray reprocessing in High Mass X-ray Binaries (HMXBs) has been reported in Aftab, Paul and Kretschmar (2019). Here we compare the eclipse flux with the out-of-eclipse flux and see the reprocessing efficiency of LMXBs as a class and make a comparison with HMXBs. Very detailed analysis of individual sources are not discussed here. We also aim to study the variability in X-ray reprocessing and its possible dependencies on the system characteristics to investigate the stability of reprocessing in a given source with multiple data sets. A list of known orbital parameters of these sources which are relevant to this work are given in Table 1. We have estimated the binary separation ( $a$ ) of each source using Kepler’s third law of motion,  $4\pi^2 a^3 = GMP^2$  (Frank, King and Raine, 2002). Where  $M$  is the total mass of the neutron star and the companion star,  $P$  is the binary period,  $G$  is the gravitational constant. We have further estimated the outer radius of the accretion disk ( $R_{\text{out}}$ ) using the relation  $R_{\text{out}} \sim 0.8 \times R_{\text{LNS}}$ , where  $R_{\text{LNS}}$  is the Roche lobe radius of the neutron star  $R_{\text{LNS}} = a \times \frac{0.49q^{-2/3}}{0.6q^{-2/3} + \ln(1+q^{-1/3})}$  (Frank, King and Raine, 2002),  $q$  is the ratio of the companion star’s mass with neutron star’s mass.

The manuscript is organized as follows. In §2 we give details of the observations and data reduction procedure with *XMM-Newton* EPIC pn, in this section we describe the spectral analysis of the eclipse and out-of-eclipse events. We discuss the results from the comparison of the eclipse and out-of-eclipse spectra of each observation and also from the comparison of the eclipse (and out-of-eclipse spectra) spectra at different epoch of the same source in §3, here we compare the X-ray reprocessing between LMXBs and HMXBs. Finally we conclude the results in §4.

Table 1: List of basic parameters of the eclipsing LMXBs analyzed in this work, where  $P_{\text{orb}}$ : Orbital period (Hr),  $q$ : Mass ratio (Ratio of companion star’s mass with the mass of neutron star)  $M_C$ : Mass of the companion ( $M_{\odot}$ ),  $i$ : inclination of the orbit with respect to the line of sight ( $^{\circ}$ ),  $d$ : Distance from Earth (kpc) ( $M_{\odot}$ ,  $R_{\odot}$ : Mass and radius of Sun respectively)

Source	$P_{\text{orb}}$ (Hr)	$q$	$M_C$ ( $M_{\odot}$ )	$i$ ( $^{\circ}$ )	$d$ (kpc)
MXB 1659–298	7.1161099(3) <sup>a1, a2</sup>	0.35-0.95 <sup>‡</sup>	(0.9±0.3) <sup>a2</sup>	(72±3) <sup>a2</sup>	(10-16) <sup>a3</sup>
EXO 0748–676	3.82410725(75) <sup>b1</sup>	0.222 <sup>+0.07b2</sup> <sub>-0.08</sub>	0.44 <sup>b2</sup>	76.5 <sup>+1.4b2</sup> <sub>-1.1</sub>	(5-11) <sup>a3</sup>
AX J1745.6–2901	8.3510389±0.0002055 <sup>c1i, c1j</sup>	≤ 0.6 <sup>c2</sup>	≤ 0.8 <sup>c2</sup>	70 <sup>+7</sup> <sub>-15</sub> <sup>c3</sup>	8.3 <sup>c4</sup>
XTE J1710–281	3.281063218(5) <sup>d1, d4</sup>	0.3 <sup>d5</sup>	0.42 <sup>*</sup>	(75-80) <sup>d2</sup>	(12-16) <sup>d3</sup>

<sup>a1</sup>(Cominsky et al., 1989), <sup>a2</sup>(Iaria et al., 2018), <sup>a3</sup>(Trigo et al., 2006)

<sup>b1</sup>(Parmar et al., 1986), <sup>b2</sup>(Knight et al., 2022)

<sup>c1i</sup>(Maeda et al., 1996), <sup>c1j</sup>(Hyodo et al., 2009), <sup>c2</sup>(Ponti et al., 2017), <sup>c3</sup>(Ponti et al., 2018), <sup>c4</sup>(Genzel et al. 2010, Bland et al. 2016, Gillessen et al. 2017)

<sup>d1</sup>(Jain and Paul, 2011), <sup>d2</sup>(Frank, King and Lasota, 1987), <sup>d3</sup>(Galloway et al., 2008), <sup>d4</sup>(Jain et al., 2022),

<sup>d5</sup>(Raman et al., 2017)

<sup>\*</sup>Derived from  $\frac{M_C}{M_{\text{NS}}} \sim 0.3$ ,  $M_{\text{NS}} \sim 1.4M_{\odot}$  (Raman et al., 2017)

<sup>‡</sup>Derived from  $M_C = (0.9 \pm 0.3)M_{\odot}$  (Iaria et al., 2018) and  $M_{\text{NS}} = (1.48 \pm 0.2)M_{\odot}$  (Ozel et al., 2012)

## 2. Observation and data analysis

*XMM-Newton* observatory consists of 3 sets of co-aligned X-ray telescopes each with an effective area of  $1500 \text{ cm}^2$ , launched in December 1999. At the focal plane of each telescope three European Photon Imaging Cameras (EPIC) are placed, two of which are made of Metal Oxide Semi-conductor (MOS) CCDs (Turner et al., 2001) and one uses pn CCDs (Strüder et al., 2001). EPIC pn instrument operates in the energy range of 0.15–15 keV and provides spectral resolution of 20–50 (E/ $\Delta$ E) and angular resolution of  $6''$  over the  $30'$  field of view. EPIC pn provides different read out modes, namely FullFrame, LargeWindow, SmallWindow, Timing mode (Lumb et al., 2012). According to the science requirements any of these modes can be selected.

We referred to Liu et al. (2007) for eclipsing LMXBs and then searched for the available EPIC pn observations in HEASARC. We found eclipse observations of four LMXBs. From these we selected a total of 17 observations, which were carried out in the Imaging mode. The log of observations along with the mode of operations are given in Table 2. We used the *XMM-Newton* Science Analysis Software (SAS) version 14.0.0 to reduce the data. The event files were extracted with the tool EVSELECT. Particle background were checked and no flares have been found in any of the observation. Events were extracted in the energy range of 0.3–12 keV. Pileup were checked with the task EPATPLOT and no pile up effect were noticed for the chosen energy range (0.3–10 keV).

We extracted images during eclipse and out-of-eclipse (OOE) of all the observations of the sources analyzed in this work. With the tool RADPROF and using the image and event files we obtained radial profiles of the sources of all the observations during eclipse and OOE phase. Figure 1 shows examples of one radial profile of each of the source. The radial profiles of MXB 1659–298 (OB ID: 0008620701), EXO 0748–676 (OB ID: 0160760801), AX J1745.6–2901 (OB ID: 0402430301) and XTE J1710–281 (OB ID: 0206990401) are shown in this figure in top left, top right, bottom left and bottom right panel respectively. The X axis shows the distance from the source in arc-sec, where zero value in this axis indicates the position of the source centroid. The Y axis denotes counts received per arc-sec<sup>2</sup> during the whole observation. The red points and green lines denote radial profile of the source in the field of view and fit of a point spread function (from the calibration files) to it respectively. The region between the Y axis and the solid line shows the source region and that between the two dashed lines shows background region used for the extraction of the source and background spectra for spectral analysis. This profile helps us to test the presence of excess emission which may be scattered from interstellar dust (during the phase for which the profile has been generated) into the line of sight. Examining the plots we observe that excess emissions are present in a few observations, but are not very close to the source. These excess emissions are present at a certain range of distances from the sources. We extracted circular source region from regions surrounding the source centroid and then extracted the background region of same size of the source, from a region which are free from any excess emission along the line of sight and also are free from any X-ray sources. Seeing the image quality we have chosen the size of the source regions. For example we have extracted the source regions with a radius of  $18''$ ,  $35''$ ,  $20''$  and  $18''$  for MXB 1659–298, EXO 0748–676, AX J1745.6–2901 and XTE J1710–281 respectively, where any excess emissions have not been observed. Similarly we have chosen the background regions from regions which are also free from excess emissions and are far away from the source. Edge of a CCD chip has been avoided for the extraction of the regions. Diffused emissions get eliminated with the background subtraction while obtaining the lightcurves and spectra. We extracted the

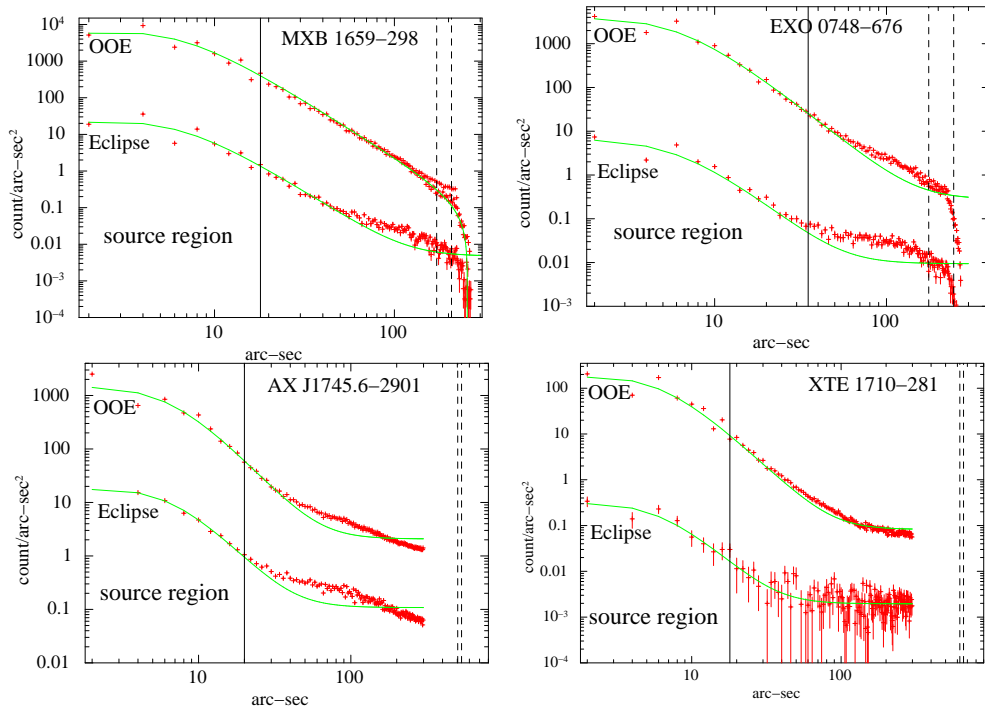


Figure 1: The radial profiles of MXB 1659-298 (top left), EXO 0748-676 (top right), AX J1745.6-2901 (bottom left) and XTE J1710-281 (bottom right) during eclipse (lower plots) and out-of-eclipse (upper plots) phase respectively. One radial profile is shown for each source. The X and Y axis shows the distance from the source in arc-sec and counts/arc-sec<sup>2</sup> received in the whole observation respectively. Zero value in the X axis indicates the position of the source centroid. The red points denote radial profile of the source in the field of view, where the green lines denote fit of a point spread function to the data. The region between Y axis and the solid line shows the source region and that between the two dashed lines describes background region.

source and background lightcurves from the single and double events (with  $PATTERN \leq 4$ ) for the full exposure time with the task EVSELECT. We then obtained background corrected source lightcurve with the task LCCORR.

### 2.1. EVENT SELECTION FROM THE LIGHTCURVES

The total lightcurves of the sources show one or more eclipse events. Figure 2 shows the eclipse and OOE events in the four lightcurves of the LMXBs, one lightcurve is shown for each of the source. The Figure shows sharp fall of intensity from out-of-eclipse to eclipse in the four sources. This suggests that the direct emission from the neutron star, inner accretion disk, boundary layer and corona is completely blocked during eclipse.

We extracted two set of events: 1) eclipse events 2) out-of-eclipse (OOE) persistent events from the event files of each observation. For that we first identified the eclipse and OOE phases from the background corrected source lightcurves of each observation. In each observation we noticed the start and end time of all the eclipse phases, then using the task GTIBUILD we generated the good time intervals of all the eclipse phases covered in the observation. Then using the task EVSELECT we extracted the eclipse events for each observation. To extract the persistent OOE events we removed the intervals of bursts and dips wherever found, and considered the intervals when the count rates are above 70% of the peak count rate. Then in a similar manner using the above tasks we extracted the persistent OOE events as we extracted the eclipse events.

### 2.2. SPECTRAL ANALYSIS

For all the observations mentioned in Table 2, we have extracted eclipse and OOE spectra. For both the eclipse and OOE phases, we extracted the spectra from the single and double events (with  $PATTERN \leq 4$ ) excluding the events which are at the edge of a CCD and at the edge to a bad pixel (with  $FLAG=0$ ). We generated response and ancillary files using the task RMFGEN and ARFGEN respectively. We used the task EVSELECT to extract the spectra from the eclipse and OOE events using corresponding response and ancillary files. We rebinned the spectra with the task SPECGROUP to have at least 25 counts per bin to be able to use  $\chi^2$  statistics.

Each observation of AX J1745.6–2901 cover 2 to 4 eclipses, whereas that of EXO 0748–676 and MXB 1659–298 cover 4 to 8 eclipses and 1 to 2 eclipses respectively. The observation of XTE J1710–281 covers only one eclipse. For each observation we extracted a single eclipse spectrum, combining the events from all the eclipses present in that observation. Similarly from each observation we extracted a single OOE spectrum, from the phases where the sources were persistent.

#### 2.2.1. ECLIPSE AND OUT-OF-ECLIPSE SPECTRA OF THE LMXBs

We have fitted eclipse and OOE spectrum of each observation of each source to see the time dependence of the characteristics of the medium surrounding the compact object. We have also obtained the composite eclipse and composite OOE spectra of MXB 1659–298, EXO 0748–676 and AX J1745.6–2901 from two, seven and seven observations respectively.

We have used XSPEC v12.11.0 (Arnaud, 1996) for the spectral fitting. The eclipse and OOE spectra were primarily fitted with power-law (XSPEC model component *powerlaw*) modified by photoelectric absorption due to gas, molecule and grain in the interstellar medium (ISM) along the line of sight (XSPEC model component *Tbabs*, Wilms et al. 2000). Though we have extracted the source and background regions where excess emissions are not observed to be present, however there is a possibility that some photons are scattered into the line of sight confronting the

surface of the dust grains present in the ISM. So to correct for the effect of X-ray scattering by the dust grains in the ISM we used the XSPEC model component *xscat* (Smith et al., 2016) and tied the value of interstellar hydrogen column density of this component with that ( $N_{\text{H}}$ ) associated with component *Tbabs*. The component *xscat* incorporates the dependence of the scattering cross-section on energy, dust and the size of the extraction region. We have chosen the default dust model (Mathis et al., 1977) that comes with the *xscat* code. The position of dust layer (*Xpos*) in a scale 0-1 is an input parameter in the component *xscat*. Where 0 corresponds to the position of the observer and while 1 is at the source. The value 0.5 is default in the component. We have initially kept it free while fitting the spectra. When its value could not be constrained then it is frozen to get best fits. Looking at the value of  $\chi^2/\text{DOF}$  i.e. reduced  $\chi^2$  ( $\chi_r^2$ ) and the residuals in  $\chi$  in the spectra, we added other components to obtain the best fit. A few of the observations showed excess low energy emission, a blackbody component was added to the model for these sources. XSPEC model component *bbodyrad* and / or *diskbb* gave the best fit of these low energy excess emissions. Excess narrow emission and / or absorption profiles were seen in a few spectra. The excess and negative residuals at specific energies were fitted with Gaussian functions. XSPEC model component *gaussian* and *gabs* have been used for emission and absorption lines respectively. For some of the observations in the OOE phase an additional component for partial covering absorption by partially ionized material (XSPEC model component *zxipcf*) was required to fit the spectra. We have also stacked the eclipse (and OOE) spectra of each source obtained from different observations with the task EPICSPECCOMBINE. Then changed the exposure of this stacked eclipse (and OOE) spectrum of each source to the total exposure of all the eclipse (and OOE) spectra available for that particular source to obtain time averaged eclipse (and OOE) spectrum. In this way we obtained a single combined eclipse (and OOE) spectrum of each source (except for XTE J1710–281, as this system has only one EPIC pn observation covering eclipse) just to see the average variation of intensity with energy. We describe the details about the spectral fitting for all the sources in the following sections.

### **MXB 1659–298:**

We have analyzed two EPIC pn observations of MXB 1659–298 (OB IDs: 0008620601, 0008620701), covering 1-2 eclipses, carried out in an interval of  $\sim 1$  year. Sidoli et al. (2001) have obtained the best fit of the persistent and eclipse spectrum of the source with *XMM-Newton* EPIC pn with a cutoff power-law, a blackbody emission, three Gaussian functions for two Fe absorption lines of 6.64 keV, 6.9 keV and 6.47 keV Fe emission line. They obtained the best fit of the eclipse spectrum with the same model. In the RGS persistent spectrum they detected absorption features from Oxygen and Neon ions with a wide range of ionization states. Trigo et al. (2006) have obtained best fit of the persistent spectrum of this source with *XMM-Newton* EPIC pn with a power-law, a blackbody component modified with absorption due to both neutral and ionized absorbers and two Gaussian functions for 6.4 keV Fe  $K_{\alpha}$  and 0.99 keV emission line modified with absorption from neutral absorber.

We first started fitting the eclipse spectrum of the observation of MXB 1659–298 with higher exposure time (OB ID: 008620701) between the two observations, we first checked the fitting with a simple power-law modified with photoelectric absorption and scattering in the ISM (Model *Tbabs* $\times$ *xscat* $\times$ *powerlaw*) in the energy range of 0.3-10 keV. We get  $\chi^2 = 94.47$  for 105 DOF and we accept this as the best fit. We obtain best fit of the eclipse spectrum of the other observation (OB ID: 0008620601) with the same model ( $\chi^2 = 21.75$  for 25 DOF)

Fitting of the OOE spectrum with higher exposure time (OB ID: 008620701) with model

*Tbabs×xscat×powerlaw* shows some low energy excess in the residuals ( $\chi^2 = 381.04$  for 110 DOF) in the energy range of 3-10 keV. The low energy excess is well fitted with the addition of component *bbodyrad*, with  $\chi^2 = 186.89$  for 108 DOF. Instead of blackbody component *bbodyrad* if we use component *diskbb*, the statistics is similar ( $\chi^2 = 186.28$  for 108 DOF), but the disk normalization is low ( $N_{\text{disk}} = 0.44$ ). Following Kubota et al. (1998) and using this normalization value and distance to the source (Trigo et al., 2006), we get a very low value of projected real inner disk radius of the accretion disk ( $<$  standard radius of a neutron star), so we do not consider *diskbb* to fit the low energy excess. With the model *Tbabs×xscat(powerlaw + bbodyrad)* we see some negative residuals in the 6–7 keV energy range. Addition of model component *gabs* for the 6.75 keV absorption line improves the fit ( $\chi^2 = 147.24$  for 106 DOF). Addition of another *gabs* component for 6.99 keV absorption line further improves the fit ( $\chi^2 = 96.85$  for 105 DOF). We accept this as the best fit for the OOE spectrum of the source.  $N_{\text{H}}$  could not be constrained and we freeze it to the value following Sidoli et al. 2001 (Table 4). In a similar manner we approached to fit the OOE spectrum of the other observation (OB ID: 008620601). We obtained best fit with the model *Tbabs×xscat×gabs(powerlaw + bbodyrad)* with  $\chi^2 = 142.21$  for 162 DOF. Addition of the emission lines in the two OOE spectra are significant at a confidence level  $> 99.99\%$ .

$N_{\text{H}}$  and  $\Gamma$  during eclipse (OOE) phase have been found in the range of  $25\text{-}26 \times 10^{20} \text{ cm}^{-2}$  ( $28\text{-}35 \times 10^{20} \text{ cm}^{-2}$ ) and  $1.52\text{-}1.57$  ( $1.75\text{-}2.07$ ) respectively. The 3-10 keV flux obtained from both OOE (and eclipse) spectra are quite similar. The OOE to eclipse flux ratio obtained in the energy range of (3 – 10) keV has been found to be 21 – 24 for the two observations. To be consistent with the observations of other three sources reported in this text we have chosen the lower energy to be 3 keV for the flux estimation. The position of the dust layer ( $X_{\text{pos}}$ ) is obtained as  $0.98^{+0.01}_{-0.05}$  for the OOE spectrum of OB ID 008620601. In other eclipse and OOE spectra of the source its value could not be constrained and it is frozen with the value 0.98. The details of the best fit models and corresponding spectral parameters are given in Table 3, 4, 5 respectively. Figure 3 shows best fit of the eclipse and OOE spectrum of MXB 1659–298 for observation which has higher exposure time (OB ID: 0008620701) between the two observations in the left and middle figure respectively. The right figure shows the time averaged combined OOE (black) and eclipse (red) spectrum of the source obtained from the two observations. Figure 4 shows the composite eclipse (left figure) and OOE spectra (right figure) respectively for the two observations, where both eclipse (OOE) spectra are observed to almost overlap.

### **EXO 0748–676:**

We have analyzed seven EPIC pn observations of EXO 0748–676 carried out over a period of  $\sim 2$  months. Each observation covers minimum 4 to maximum 8 eclipses. Triplets of thermonuclear X-ray bursts (Boirin et al., 2007), X-ray burst reprocessing (Paul et al., 2012), orbit to orbit variations of the X-ray dips and orbital modulations of the optical light curves (Raman et al., 2017) have been reported from these observations. Raman et al. 2017 reported the source to be in the hard state during these seven observations. Cottam et al. (2008) reported gravitationally redshifted absorption lines in the 28 burst spectra of this source with *XMM-Newton* RGS. Raman et al. (2017) have obtained the best fit of the persistent *XMM-Newton* spectra with a power-law modified with neutral and partial covering ionized absorption along with two Gaussian functions for 0.569 keV (fixed) and 0.915 (fixed) keV emission lines modified with photoelectric absorption along the line of sight due to neutral absorber. Increase of covering fraction of the ionized absorber and a decrease in the ionization parameter has been observed from persistent emission to dipping (Trigo et al. 2006, Raman et al. 2017).



We first checked the fitting of the eclipse spectrum of EXO 0748–676 which has highest exposure time amongst the seven observations (OB ID: 0160760301). The model  $Tbabs \times xscat \times powerlaw$  gives a  $\chi^2 = 245.38$  for 88 DOF in the energy range of 0.3-10 keV. We see some low energy excess and use the component  $bbodyrad$  to account for it, the fit is improved with  $\chi^2 = 112.96$  for 86 DOF. Since during eclipse the inner accretion disk is expected to be blocked by the companion, so we use blackbody component  $bbodyrad$  instead of component  $diskbb$ . We see an excess  $\sim 0.5$  keV, addition of an emission line of 0.55 keV with model component  $gaussian$  significantly improves the fit ( $\chi^2 = 97.58$  for 84 DOF), so we report model  $Tbabs \times xscat (powerlaw + bbodyrad + gaussian)$  as the best fit model for this eclipse spectrum. In a similar manner we fitted the other eclipse spectra of this source. Other six observations required 1 – 5 emission lines for the best fits. For example the observation with OB ID: 0160760201 required five emission lines for the best fit. Fitting this spectrum with the model  $Tbabs \times xscat (powerlaw + bbodyrad)$ , we get a  $\chi^2 = 191.98$  for 66 DOF with some positive residuals at specific energies below 2 keV and near 6.4 keV. When we add component  $gaussian$  for these excess, the fit gradually improves. For example adding this component ( $gaussian$ ) for emission lines at 0.54 keV, 0.89 keV, 1.39 keV, 1.80 keV and 6.44 keV we get  $\chi^2$  of 109.64, 79.23, 71.60, 64.20 and 56.51 for 63, 61, 59, 57 and 55 DOF respectively. In the similar approach we obtain the best fit of the other eclipse spectra of this source. Addition of the lines are significant at a confidence level  $>99.99\%$ . Except for OB ID 0160760101,  $N_H$  could not be constrained and it is frozen with  $3 \times 10^{20} \text{ cm}^{-2}$  to obtain best fit of the eclipse spectra.

Fitting of the OOE spectrum of OB ID: 0160760301 having highest exposure amongst the seven OOE observations with the simple model  $Tbabs \times xscat \times powerlaw$  gives  $\chi^2 = 90417$  for 176 DOF in the energy range of 0.3-10 keV. We observe some low energy excess and positive residuals in 5 – 6 keV energy range. We add the blackbody component  $diskbb$  to account for the low energy excess, the fit is improved with  $\chi^2 = 2269$  for 174 DOF. Adding 0.59 keV emission line with component  $gaussian$  makes the fit better ( $\chi^2 = 1269$  for 171 DOF). We observe some continuous negative residuals at low energies, to account for it we add a partial covering absorption model by partially ionized material (component  $zxipcf$ ) following Raman et al. (2017). The fit is significantly improved with  $\chi^2 = 142.80$  for 168 DOF. Instead of ionised absorption component ( $zxipcf$ ), if we use partial covering absorption model by neutral material (component  $pcfabs$ ), the  $\chi^2$  is 187.81 for 169 DOF. For this reason we use the component  $zxipcf$  instead of  $pcfabs$ . So we accept the model  $Tbabs \times xscat \times zxipcf (powerlaw + diskbb) + Tbabs \times xscat \times gaussian$  as the best fit model for this eclipse spectrum. We use  $diskbb$  component to account for the blackbody radiation for the OOE spectra, as the inner disk is visible when the compact object is out of eclipse. We have obtained the best fit of the OOE spectra of other observations of this source in a similar manner. In the three observations we required  $\sim 6.8$  keV absorption line (OB ID: 0160760401, 0160760601 and 0160760801). Addition of the emission line is significant at a confidence level  $>99.99\%$ . For the best fit of the two observations (OB ID: 0160760401 and 0160760801) no emission line is observed. In one observation (OB ID: 0160760101) we have observed a significant positive residual at low energies even after fitting with the model  $Tbabs \times xscat \times zxipcf \times gabs (powerlaw + diskbb) + Tbabs \times xscat \times gaussian$  ( $\chi^2$  400.14 and 168 DOF). Adding a blackbody component  $bbodyrad$  significantly improves the fit ( $\chi^2$  195.87 for 166 DOF), we accept this fit as the best fit for this observation during OOE phase ( $Tbabs \times xscat \times zxipcf \times gabs (powerlaw + diskbb + bbodyrad) + Tbabs \times xscat \times gaussian$ ).

The Temperature associated with component  $bbodyrad$  is high ( $4.16^{+0.72}_{-0.44}$  keV) with a small value of normalization ( $0.08^{+0.03}_{-0.03}$ ).  $N_H$  and  $\Gamma$  during eclipse (OOE) phase have been found in the range of  $3-4 \times 10^{20} \text{ cm}^{-2}$  ( $11 \times 10^{20} \text{ cm}^{-2}$  frozen) and 0.87-1.16 (1.27-2.24) respectively. The (3-

10) keV flux values are quite similar in all the observations during eclipse. The OOE to eclipse flux ratios have been found in the range of  $\sim(43-54)$  for the seven observations. The ionized absorbers have been found to cover (55-92)% (as CvF, the covering factor  $\sim 0.55-0.92$ ) of the source emission during out-of-eclipse. The position of the dust layer ( $X_{\text{pos}}$ ) could not be constrained and is frozen at 0.98 to obtain the best fit of the eclipse and OOE spectra. The details of the best fit model and spectral parameters are given in Table 3, 4, 5 and 6 respectively. Figure 5 shows best fit of the eclipse (left) and OOE (middle) spectrum of EXO 0748–676 for observation which has highest exposure time among the seven observations. The right panel of this figure shows the time averaged combined OOE (black) and eclipse (red) spectra obtained from combining the seven OOE and eclipse observations respectively. Figure 6 shows the composite eclipse (top left) and OOE (top right and bottom) spectra of the seven observations. The OOE spectra obtained including and excluding the dips intervals are shown in the top right panel and bottom panel respectively.

### AX J1745.6–2901:

We have analyzed seven EPIC pn observations of AX J1745.6–2901 carried out over a period of  $\sim 8$  and half years. Each observation covers minimum 2 to maximum 4 eclipses. We first checked the fitting of the eclipse spectrum of the hard state observation of the source which has the highest exposure time (OB ID: 0723410501) during eclipse in the energy range of 2-10 keV, as below 2 keV the photon counts are almost nil. The best fit was obtained with simple model  $Tbabs \times xscat \times powerlaw$  with  $\chi^2 = 10.74$ , for 10 DOF. In a similar manner the best fit of the eclipse spectra of other hard-state observations were obtained with the same model stated above. The OOE spectrum of the observation (OB ID: 0723410501) were also best fitted with the simple model ( $Tbabs \times xscat \times powerlaw$ ) with  $\chi^2 = 74.65$  for 99 DOF. Best fit of the OOE spectrum of the other two observations were also obtained with this model.  $N_{\text{H}}$  and  $\Gamma$  during eclipse (OOE) phase have been found in the range of  $(9.39 - 19.50) \times 10^{22} \text{ cm}^{-2}$  ( $(17.15 - 19.50) \times 10^{22} \text{ cm}^{-2}$ ) and 2.05 – 2.65 (1.65 – 1.89) respectively. Ponti et al. (2015) reported an absorbed power-law model for the best fit of the hard state *XMM-Newton* persistent spectra of the source. The details of the best fit model and spectral parameters are given in Table 3, 4, 5 respectively. The left panel of Figure 8 shows best fit of the eclipse spectrum of AX J1745.6–2901 for observation which has highest exposure time during eclipse among the three hard state observations, the middle panel shows corresponding OOE spectrum. The right panel shows the time averaged combined OOE (black) and eclipse (red) spectrum of the source in hard state obtained from the three OOE and eclipse observations respectively.

The eclipse spectrum of the soft state observation (OB ID: 0762250301) of AX J1745.6–2901 with highest exposure time was first fitted with model  $Tbabs \times xscat \times powerlaw$  in the energy range of 2-10 keV, the fit gives a  $\chi^2$  42.53 for DOF 50. We accept this as the best fit. For the other two observations also best fit of the eclipse spectra are obtained with the same model. The OOE spectrum of the observation (OB ID: 0762250301) was first fitted with the simple model ( $Tbabs \times xscat \times powerlaw$ ) in the energy range of 0.3-10 keV, a  $\chi^2$  383.95 for DOF 110 was observed. Some low energy excess and both negative and positive residuals are observed in 6-7 keV energy range. Addition of blackbody component  $bbbodyrad$  improves the fit ( $\chi^2$  269.08 for DOF 108). Instead of  $bbbodyrad$  if we use  $diskbb$  component then the disk normalization is very low (0.43). Following Kubota et al. (1998) and from this normalization and distance to the source, the value of the apparent inner disk radius is estimated to be significantly smaller than the radius

of the neutron star. So we accept component *bbodyrad* to fit the low energy excess in this spectrum. Adding 6.71 keV and 6.96 keV absorption lines we get better fits ( $\chi^2$  220.43 and 139.63 for 107 and 106 DOF respectively). Addition of an emission line of 6.4 keV finally gives the best fit ( $Tbabs \times xscat \times gabs_1 \times gabs_2 (powerlaw + bbodyrad + gaussian)$ ) with  $\chi^2$  132.08 for 105 DOF. The addition of the absorption and emission lines is significant at a confidence level >99.99%.

In a similar manner we fitted the OOE spectra of the other three soft state observations. The best fit of the two OOE spectra (OB ID: 0402430401, 0724210201) were obtained with the same model except the emission line. The best fit of the OOE spectrum of the other observation (OB ID: 0402430301) was obtained with the model  $Tbabs \times xscat \times gabs_1 \times gabs_2 \times powerlaw$ .  $N_H$  and  $\Gamma$  during eclipse (OOE) phase have been found in the range of  $(17.14-19.23) \times 10^{22} \text{ cm}^{-2}$  ( $(16.35-20.58) \times 10^{22} \text{ cm}^{-2}$ ) and 3.03–3.83 (1.65–2.36) respectively.  $\Gamma$  is higher during eclipse phases compared to OOE in all the hard and soft state observations of AX J1745.6–2901. The OOE to eclipse flux ratio in the energy range of (3–10) keV is in the range of  $\sim(6-10)$  for the source. We have detected Fe XXV and Fe XXVI absorption lines in the soft states but did not find any absorption feature in the hard states (upper limits of strength of Fe XXV and Fe XXVI absorption lines in hard state observations are 0). Ponti et al. (2015) also has observed these absorption lines only in soft states in this source. The position of the dust layer ( $X_{pos}$ ) could not be constrained and is frozen at 0.98 to obtain the best fit of the eclipse and OOE spectra of the source in both soft and hard states. The best fit model and the details of the best fit spectral parameters of the combined eclipse and OOE spectra of AX J1745.6–2901 are given in Table 3, 4 and 5 respectively. Figure 7 and 8 show the eclipse (left figures) and OOE spectra (middle figures) of AX J1745.6–2901 for the soft and hard state observations respectively. The right figures show the time averaged combined OOE (black) and eclipse (red) spectrum of the source obtained from the three hard state and four soft state observations respectively.

Figure 9 shows the composite eclipse (left figure) and out-of-eclipse (right figure) spectra respectively for the soft and hard state observations of AX J1745.6–2901. The intensity of the four soft-state eclipse (OOE) spectra (black, red, green, blue) are seen to be higher compared to three hard-state eclipse (OOE) spectra (orange, grey, magenta). Intensity of a soft-state OOE spectrum (blue solid star, right figure) is more than 5 times lower than three other soft-state OOE spectra. Corresponding to this observation, the intensity drops by similar factor in the reprocessed eclipse spectrum (left figure) also.

### **XTE J1710–281:**

We have analyzed one EPIC pn observation of XTE J1710–281, which covers single eclipse. Younes et al. (2009) reported the *XMM-Newton* persistent and dip spectrum fitting with a simple power-law modified for line of sight absorption due to neutral materials along with a partial covering absorption due to neutral absorber. They obtained best fit of these spectra when they replace the partial covering absorption due to neutral absorber with that due to ionized absorber. The parameters of the ionized absorber could not be constrained for the persistent spectrum. They have not obtained any signature of highly ionized Fe lines. Raman et al. (2018) obtained best fit of the time average *Chandra* spectrum with a simple power-law modified with line of sight absorption due to neutral material and partially covered ionized materials. To get the best fit of the *Suzaku* spectrum they required three Gaussian functions, two for 6.6 keV and 7.01 keV absorption lines and one for 0.72 keV emission line. Highly ionized Fe line has been obtained for the first time in the source (Raman et al. 2018). They have also obtained intensity resolved

spectral fit with *Chandra* and *Suzaku*, and observed an increase of column density of the ionized absorber and a decrease of ionization state from the persistent to dip spectra.

The eclipse spectrum has very limited statistics leading to only a few bins in the binned spectrum. We fitted the OOE spectrum first with a simple *powerlaw* component modified with the line of photoelectric absorption and scattering in the ISM (*Tbabs* $\times$ *xscat* $\times$ *powerlaw*,  $\chi^2 = 197.74$  for 150 DOF). When we add partial covering absorption due to neutral absorber or that due to ionized absorber, the fit does not improve ( $\chi^2$  of 198.32 and 195.51 for 148 and 147 DOF respectively). So we accept the simple model stated above as the best fit model. Only for the estimation of the flux ratio between the OOE and eclipse phases we fitted the eclipse spectrum with model *Tbabs* $\times$ *xscat* $\times$ *powerlaw* and the OOE to eclipse flux ratio has been found to be  $\sim 129$ . The position of the dust layer (*Xpos*) could not be constrained and is frozen at 0.98 to obtain the best fit of the spectra. The details of the spectral parameters of the OOE spectrum of this source are given in Table 4. The  $N_{\text{H}}$  is similar to that obtained in the two observations of MXB 1659–298. Figure 10 shows both eclipse and OOE spectra of XTE J1710–281 in one panel.

### 2.3. To investigate the effect of dust scattered emission in the eclipse (OOE) spectra

To check the effect of dust scattering in the eclipse (OOE) spectra we have fitted all the spectra including and excluding the dust scattering component *xscat* and compared the spectral parameters. We have not observed any change. To investigate further we have also obtained the low energy X-ray flux in 0.3–3 keV energy range including and excluding the component *xscat*, since the dust scattering of X-ray photons mostly affect the photon count distribution with respect to energy in low energy X-ray regime, as the dust scattering cross section  $\propto E^{-2}$  (Smith et al., 2016). We obtain same flux including and excluding the component *xscat* in 0.3–3 keV energy range (Table 7). This also confirms that the emission received during eclipses are free from dust scattered emission and are from the binary system only.

To check further the presence of dust along and /or close to the line of sight, we have plotted the line of sight column density ( $N_{\text{H}}$ ) with OOE to eclipse flux ratio for all the observations (Figure 11) except that of XTE J1710–281, as for this source the statistics of the eclipse spectrum is poor. We do not observe correlation between the  $N_{\text{H}}$  and the flux ratio, which indicates negligible effect of dust scattered photons from a region along and /or close to the line of sight. In the source EXO 0748–676, thermonuclear X-ray bursts have been observed during eclipses (Parmar et al. 1986, Parmar et al. 1985, Wolff et al. 2009) which provides an evidence that the emission observed during eclipses are the reflection from a region which is close to the neutron star. Otherwise if the emission during eclipses were due to the reflection from the dust distributed in a larger region, then the bursts would be delayed by different amount from different dust layers, hence would not be detected. There is also an indication of detection of thermonuclear X-ray bursts in MXB 1659–298 during eclipse (Wijnands et al., 2002), but to be consistent they have analyzed the bursts outside eclipse and dips in that work.

## 3. Discussion

During eclipses in LMXB systems the direct emission is completely blocked by the companion and the detected X-rays are the reprocessed X-rays from the surrounding medium. In

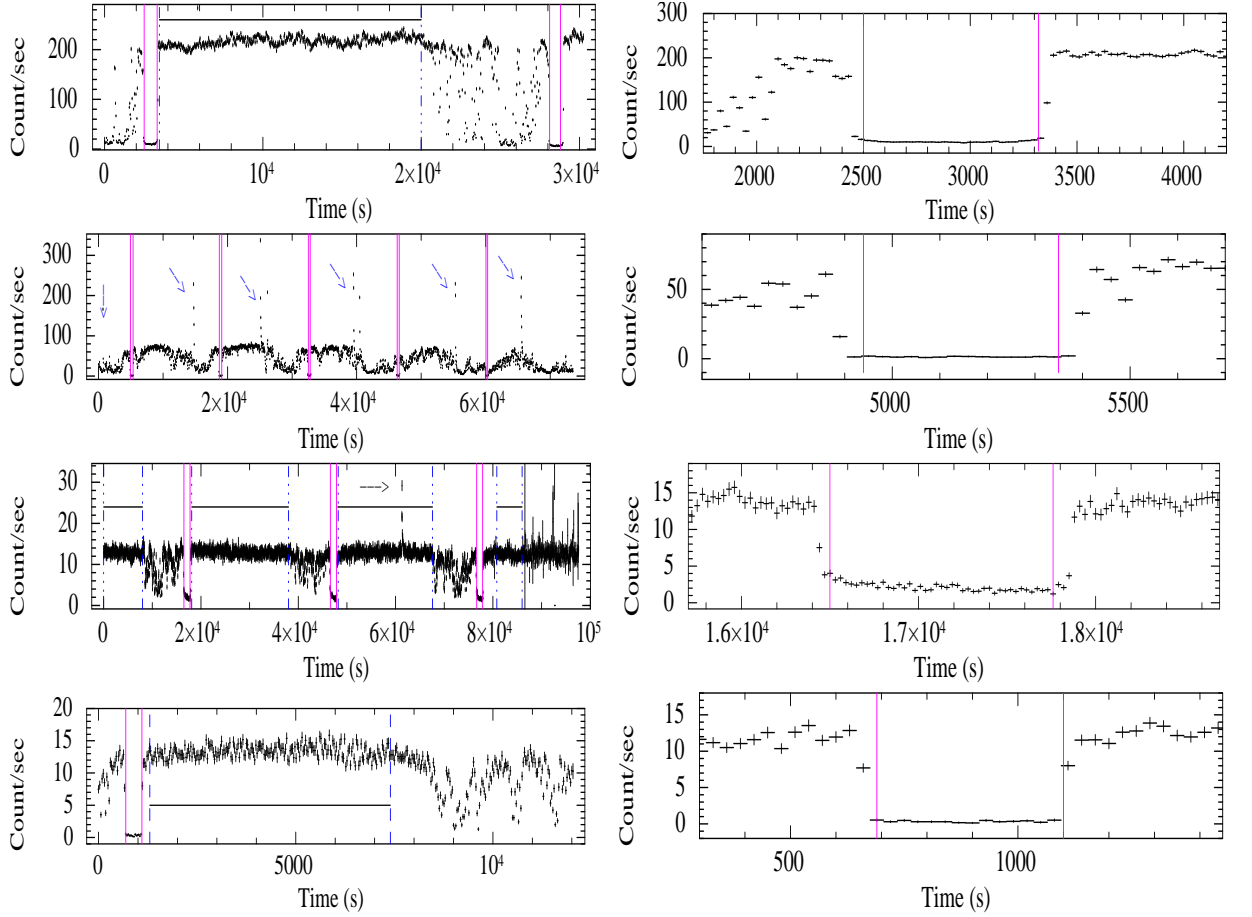


Figure 2: The eclipse and OOE events in the four lightcurves of the LMXBs; one lightcurve is shown for each of the sources. The four lightcurves are of MXB 1659–298 (OB ID: 0008620701, top-most panels), EXO 0748–676 (OB ID: 0160760401, panels in the second row), AX J1745.6–2901 (OB ID: 0402430401, panels in the third row) and XTE J1710–281 (OB ID: 0206990401, bottom-most panels). **Left figures (Full lightcurves):** The events within pink solid (blue dot-dashed/dashed) lines in the light-curves show eclipse (OOE) events. The eclipse (OOE) spectrum has been obtained from these eclipse (OOE) events. Bursts (wherever found), dips and count rate less than 70% of the peak count rate after excluding the bursts have been removed for the extraction of the OOE spectra. **Right figures (Eclipse lightcurves):** Zoomed view of an eclipse event in the same lightcurves. Similar extraction of the eclipse and OOE spectra has been done for other observations of each of the sources. A single eclipse (OOE) spectrum has been obtained from multiple eclipse (OOE) spectra of a source. Combined eclipse (OOE) spectrum of a source has been obtained by stacking all the eclipse (OOE) spectra of all the observations of a particular source.

Table 2: The EPIC pn observation log of four eclipsing LMXB systems. All the observations were carried out in IMAGING mode.

Source	Observation ID	Date of observation	Submode	Spectral state	No. of eclipses
MXB 1659–298	0008620601	2000-03-22	PrimeSmallWindow	Soft	1
MXB 1659–298	0008620701	2001-02-20	PrimeSmallWindow	Soft	2
EXO 0748–676	0160760101	2003-09-19	PrimeSmallWindow	Faint-hard <sup>c</sup>	7
EXO 0748–676	0160760201	2003-09-21	PrimeSmallWindow	Faint-hard <sup>c</sup>	7
EXO 0748–676	0160760301	2003-09-23	PrimeSmallWindow	Faint-hard <sup>c</sup>	8
EXO 0748–676	0160760401	2003-09-25	PrimeSmallWindow	Faint-hard <sup>c</sup>	5
EXO 0748–676	0160760601	2003-10-21	PrimeSmallWindow	Faint-hard <sup>c</sup>	4
EXO 0748–676	0160760801	2003-10-25	PrimeSmallWindow	Faint-hard <sup>c</sup>	4
EXO 0748–676	0160761301	2003-11-12	PrimeSmallWindow	Faint-hard <sup>c</sup>	7
AX J1745.6–2901	0402430301	2007-04-01	PrimeFullWindow	Soft <sup>a</sup>	3
AX J1745.6–2901	0402430401	2007-04-03	PrimeFullWindow	Soft <sup>a</sup>	3
AX J1745.6–2901	0723410301	2014-02-28	PrimeFullWindow	Hard <sup>b</sup>	2
AX J1745.6–2901	0723410401	2014-03-10	PrimeFullWindow	Hard <sup>b</sup>	2
AX J1745.6–2901	0723410501	2014-04-02	PrimeFullWindow	Hard <sup>b</sup>	2
AX J1745.6–2901	0724210201	2013-08-30	PrimeFullWindow	Soft <sup>a</sup>	2
AX J1745.6–2901	0762250301	2015-09-27	PrimeFullWindow	Soft	4
XTE J1710–281	0206990401	2004-02-22	PrimeFullWindow	Soft	1

<sup>a</sup>Ponti et al. (2015), <sup>b</sup>Ponti et al. (2018), <sup>c</sup>Raman et al. (2017)

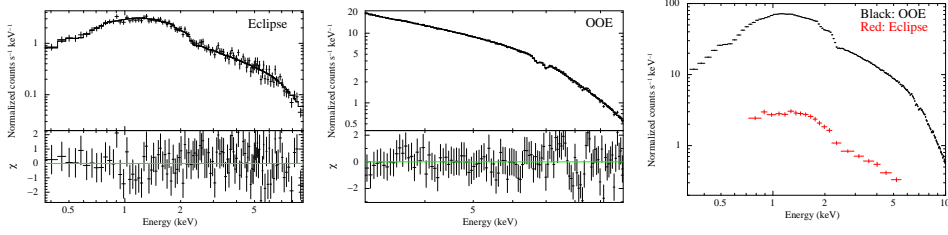


Figure 3: Left and middle figure show best fit of the eclipse and OOE spectrum of MXB 1659–298 respectively having highest exposure time between the two soft-state observations (OB ID: 0008620701). The bottom panels in these two figures are the contribution of  $\chi$  towards each bin for the best fit. The right figure shows both time averaged combined eclipse (red) and OOE (black) spectra of MXB 1659–298 obtained from two observations.

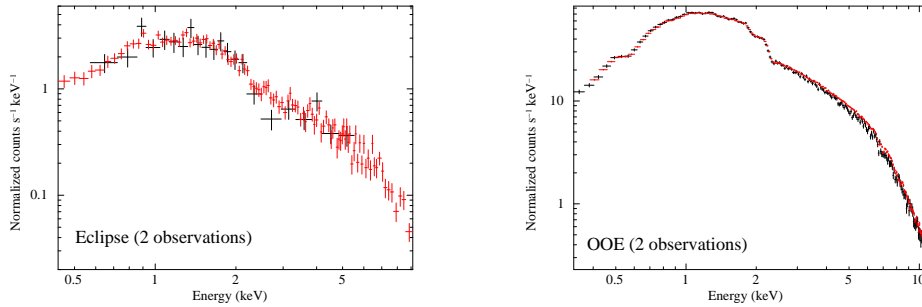


Figure 4: Composite eclipse spectra (left) and OOE spectra (right) of MXB 1659–298 for the two EPIC-pn observations, observed in soft-state.

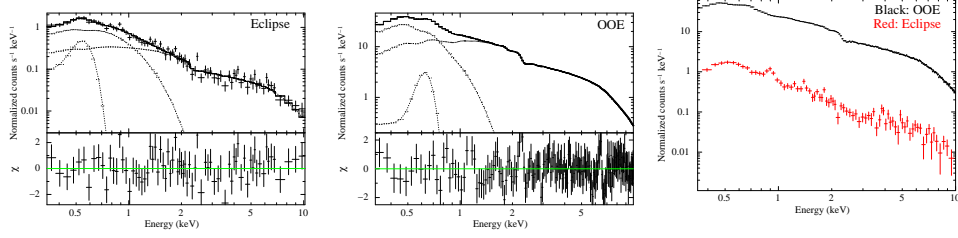


Figure 5: Eclipse (left figure) and OOE (middle figure) spectrum of EXO 0748–676 respectively with highest exposure time amongst the seven hard-state observations (OB ID: 0160760301). The bottom panels in these two figures are the contribution of  $\chi$  towards each bin for the best fit. The right figure shows both time averaged combined eclipse (red) and OOE (black) spectra of EXO 0748–676 obtained from seven observations.

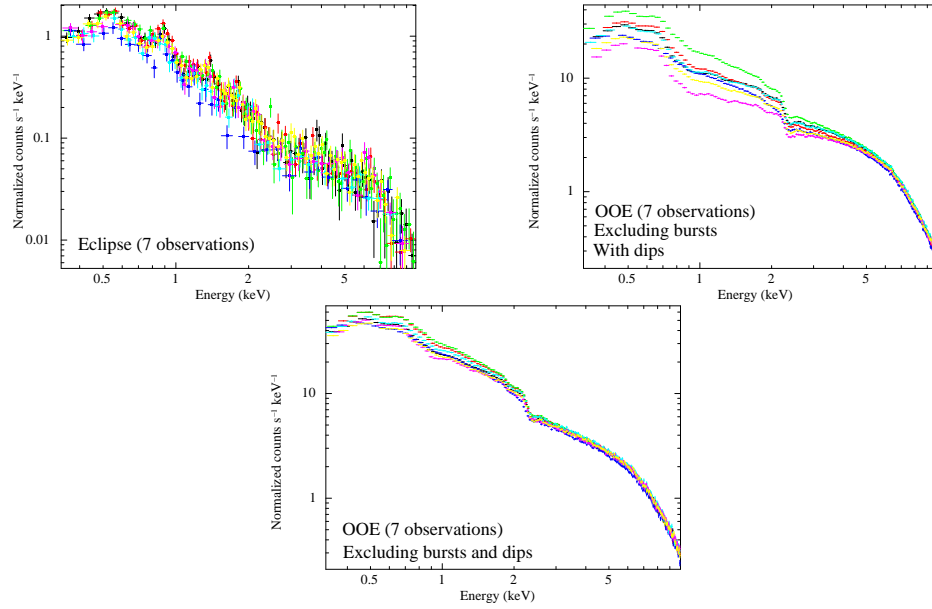


Figure 6: Composite eclipse spectra (top left), OOE spectra including dips intervals (top right), OOE spectra excluding the dips intervals (bottom panel) of EXO 0748–676 for the seven EPIC-pn observations, observed in hard-state.

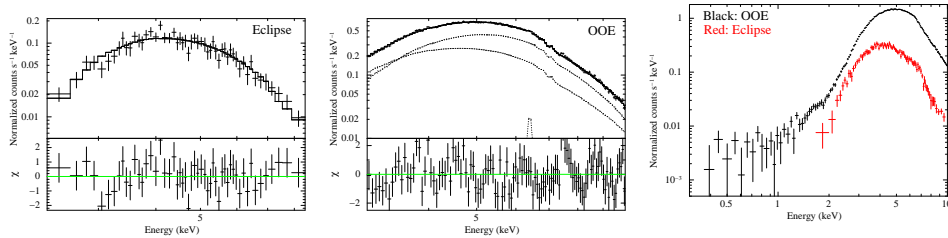


Figure 7: Eclipse (left figure) and OOE (middle figure) spectrum of AX J1745.6–2901 (OB ID: 0762250301) with highest exposure time amongst the four soft-state observations. The bottom panels in these two figures are the contribution of  $\chi$  towards each bin for the best fit. The right figure shows both time averaged combined eclipse (red) and OOE (black) spectra of AX J1745.6–2901 obtained from four soft-state observations.

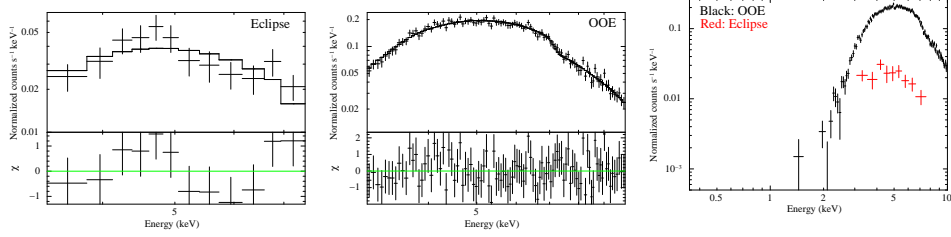


Figure 8: Eclipse (left figure) spectrum of AX J1745.6–2901 (OB ID: 0723410501) with highest exposure time amongst the three hard-state observations and corresponding OOE (middle figure) spectrum. The bottom panels in these two figures are the contribution of  $\chi$  towards each bin for the best fit. The right figure shows both time averaged combined eclipse (red) and OOE (black) spectra of AX J1745.6–2901 obtained from three hard-state observations.

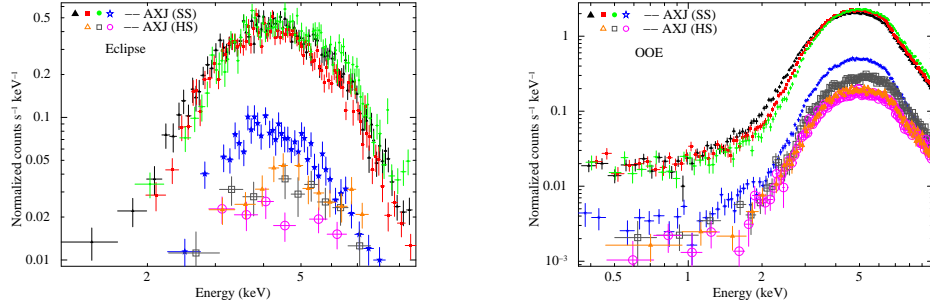


Figure 9: Composite eclipse (left) and OOE (right) spectra of AX J1745.6–2901 for seven EPIC-pn observations. The soft-state spectra are represented with solid triangle (black), box (red), circle (green) and star (blue) marker and the hard-state spectra are shown with hollow box (grey), circle (magenta) and triangle (orange) marker in both the figures. The intensity of the soft-state spectra are higher compared to that of the hard-state spectra in both phases. Intensity of a soft-state OOE spectrum (right figure, blue solid star) is more than five times lower than that of the three other soft-state OOE spectra. Corresponding to this observation, the intensity drops by similar factor in the reprocessed eclipse spectrum (left figure, blue solid star) also.

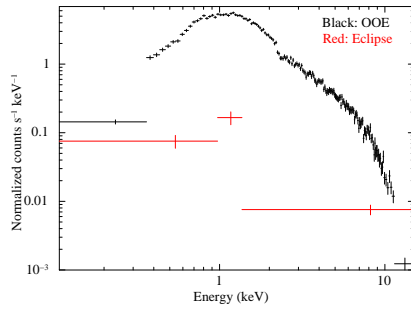


Figure 10: Eclipse (red) and OOE (black) spectra of XTE 1710–281



Table 3: The exposure times and best fit models of the eclipse and OOE spectra of four eclipsing LMXBs. ( $T_{eff}$ : Effective exposure (s), MXB: MXB 1659–298, EXO: EXO 0748–676, AXJ: AX J1745.6–2901, XTE: XTE J1710–281, E: Eclipse, OOE: Out-of-eclipse,  $pow$ : powerlaw,  $ga$ : Gaussian)

Source	State	OB ID	Phase	$T_{eff}$	Best fit model
MXB	soft	0008620601	OOE	1291	$Tbabs \times xscat \times gabs(pow + bbodyrad)$
MXB	soft		E	98	$Tbabs \times xscat \times pow$
MXB	soft	0008620701	OOE	11747	$Tbabs \times xscat \times gabs_1 \times gabs_2(pow + bbodyrad)$
MXB	soft		E	1058	$Tbabs \times xscat \times pow$
EXO	hard	0160760101	OOE	16378	$Tbabs \times xscat \times zxcipcf \times gabs(pow + diskbb + bbodyrad) + Tbabs \times xscat \times ga$
EXO	hard		E	2361	$Tbabs \times xscat(pow + bbodyrad + ga_1 + ga_2 + ga_3)$
EXO	hard	0160760201	OOE	16665	$Tbabs \times xscat \times zxcipcf(pow + diskbb) + Tbabs \times xscat \times ga$
EXO	hard		E	2340	$Tbabs \times xscat(pow + bbodyrad + ga_1 + ga_2 + ga_3 + ga_4 + ga_5)$
EXO	hard	0160760301	OOE	26747	$Tbabs \times xscat \times zxcipcf(pow + diskbb) + Tbabs \times xscat \times ga$
EXO	hard		E	2662	$Tbabs \times xscat(pow + bbodyrad + ga)$
EXO	hard	0160760401	OOE	14883	$Tbabs \times xscat \times zxcipcf \times gabs(pow + diskbb)$
EXO	hard		E	1156	$Tbabs \times xscat(pow + bbodyrad + ga)$
EXO	hard	0160760601	OOE	9094	$Tbabs \times xscat \times zxcipcf \times gabs(pow + diskbb) + Tbabs \times xscat \times ga$
EXO	hard		E	1373	$Tbabs \times xscat(pow + bbodyrad + ga)$
EXO	hard	0160760801	OOE	8900	$Tbabs \times xscat \times zxcipcf \times gabs(pow + diskbb) + Tbabs \times xscat \times ga$
EXO	hard		E	1338	$Tbabs \times xscat(pow + bbodyrad + ga_1 + ga_2 + ga_3 + ga_4)$
EXO	hard	0160761301	OOE	15954	$Tbabs \times xscat \times zxcipcf(pow + diskbb)$
EXO	hard		E	2327	$Tbabs \times xscat(pow + bbodyrad + ga_1 + ga_2 + ga_3)$
AXJ	soft	0402430301	OOE	47261	$Tbabs \times xscat \times gabs_1 \times gabs_2 \times pow$
AXJ	soft		E	3292	$Tbabs \times xscat \times pow$
AXJ	soft	0402430401	OOE	43498	$Tbabs \times xscat \times gabs_1 \times gabs_2(pow + bbodyrad)$
AXJ	soft		E	3244	$Tbabs \times xscat \times pow$
AXJ	soft	0724210201	OOE	29217	$Tbabs \times xscat \times gabs_1 \times gabs_2(pow + bbodyrad)$
AXJ	soft		E	2109	$Tbabs \times xscat \times pow$
AXJ	soft	0762250301	OOE	83655	$Tbabs \times xscat \times gabs_1 \times gabs_2(pow + bbodyrad + ga)$
AXJ	soft		E	4119	$Tbabs \times xscat \times pow$
AXJ	hard	0723410301	OOE	19455	$Tbabs \times xscat \times pow$
AXJ	hard		E	1578	$Tbabs \times xscat \times pow$
AXJ	hard	0723410401	OOE	31239	$Tbabs \times xscat \times pow$
AXJ	hard		E	2208	$Tbabs \times xscat \times pow$
AXJ	hard	0723410501	OOE	18724	$Tbabs \times xscat \times pow$
AXJ	hard		E	2218	$Tbabs \times xscat \times pow$
XTE	soft	0206990401	OOE	5465	$Tbabs \times xscat \times pow$
XTE	soft		E	367	poor statistics <sup>*</sup>

\*: fitted with the model  $Tbabs \times xscat \times pow$  only for the purpose of estimation of flux.

Table 4: The best fit parameters of the eclipse and OOE spectra of the four eclipsing LMXBs, where MXB: MXB 1659–298, EXO: EXO 0748–676, AXJ: AX J1745.6–2901, XTE: XTE J1710–281, E: Eclipse, OOE: Out-of-eclipse,  $N_H$ : Line of sight equivalent hydrogen column density,  $\Gamma$ : Powerlaw photon index,  $T_{BB}$ : Blackbody temperature (associated with component *bbodyrad*),  $T_{in}$ : Inner accretion disk temperature (associated with component *diskbb*),  $N_{bbrd}$ : Blackbody normalization associated with model component *bbodyrad* ( $(\frac{R_{km}}{D_{10kpc}})^2$ ),  $N_{disk}$ : Blackbody normalization associated with model component *diskbb* ( $(\frac{R_{in}}{D_{10}})^2 \cos\theta$ ), DOF: Degrees of freedom. Flux ratio gives the ratio of (3–10 keV) flux in the OOE phase with that in eclipse phase.  $R_{km}$ ,  $R_{in}$  and  $\theta$  are the radius of the blackbody emitting region, apparent inner accretion disk radius and angle of the normal to the disk plane with the line of sight. The errors are given with 90% confidence limit. frz: Frozen

Source	State	OB ID	Phase	$N_H$ ( $10^{22} \text{ cm}^{-2}$ )	$\Gamma$	$T_{BB}$ or $T_{in}$ (keV)	$N_{bbrd}$ or $N_{disk}$	$\chi^2/\text{DOF}$	Flux (3–10 keV) ( $10^{-11} \text{ ergs cm}^{-2} \text{ sec}^{-1}$ )	Flux ratio
MXB	soft	0008620601	OOE	$0.28^{+0.01}_{-0.01}$	$1.75^{+0.04}_{-0.03}$	$1.10^{+0.06}_{-0.05}$ [ $T_{BB}$ ]	$12.06^{+2.01}_{-2.04}$	142.21/162	55.90	21.09
			E	$0.25^{+0.08}_{-0.07}$	$1.52^{+0.21}_{-0.20}$	–	–	21.75/25	2.65	
MXB	soft	0008620701	OOE	0.35 (frz)	$2.07^{+0.18}_{-0.13}$	$1.75^{+0.12}_{-0.15}$ [ $T_{BB}$ ]	$2.77^{+0.54}_{-0.36}$	96.85/105	61.14	23.88
			E	$0.26^{+0.02}_{-0.02}$	$1.57^{+0.05}_{-0.05}$	–	–	94.47/105	2.48	
EXO	hard	0160760101	OOE	0.11 (frz)	$2.24^{+0.11}_{-0.17}$	$0.09^{+0.00}_{-0.01}$ [ $T_{in}$ ]	180055 (frz)	195.87/166	17.84	54.06
			E	$0.04^{+0.01}_{-0.01}$	$1.04^{+0.17}_{-0.18}$	$0.21^{+0.02}_{-0.03}$ [ $T_{BB}$ ]	24 (frz)	67.14/70	0.33	
EXO	hard	0160760201	OOE	0.11 (frz)	$1.31^{+0.01}_{-0.01}$	$0.14^{+0.01}_{-0.01}$ [ $T_{in}$ ]	$18971^{+4210}_{-3164}$	234.28/167	14.77	49.23
			E	0.03 (frz)	$1.14^{+0.15}_{-0.15}$	$0.19^{+0.01}_{-0.01}$ [ $T_{BB}$ ]	68 (frz)	56.51/55	0.30	
EXO	hard	0160760301	OOE	0.11 (frz)	$1.34^{+0.01}_{-0.01}$	$0.15^{+0.00}_{-0.01}$ [ $T_{in}$ ]	$18073^{+2777}_{-3271}$	142.81/168	15.82	46.53
			E	0.03 (frz)	$1.06^{+0.14}_{-0.14}$	$0.17^{+0.01}_{-0.01}$ [ $T_{BB}$ ]	$155^{+42}_{-32}$	97.58/84	0.34	
EXO	hard	0160760401	OOE	0.11 (frz)	$1.39^{+0.02}_{-0.02}$	$0.20^{+0.01}_{-0.01}$ [ $T_{in}$ ]	$13894^{+9526}_{-6213}$	166.44/150	13.84	49.43
			E	0.03 (frz)	$0.87^{+0.18}_{-0.18}$	$0.13^{+0.00}_{-0.00}$ [ $T_{BB}$ ]	389 (frz)	46.29/34	0.28	
EXO	hard	0160760601	OOE	0.11 (frz)	$1.32^{+0.02}_{-0.02}$	$0.15^{+0.01}_{-0.01}$ [ $T_{in}$ ]	$14310^{+2666}_{-2129}$	219.38/166	15.64	53.93
			E	0.03 (frz)	$0.92^{+0.17}_{-0.18}$	$0.15^{+0.01}_{-0.01}$ [ $T_{BB}$ ]	$234^{+91}_{-62}$	37.90/40	0.29	
EXO	hard	0160760801	OOE	0.11 (frz)	$1.27^{+0.01}_{-0.01}$	$0.14^{+0.01}_{-0.01}$ [ $T_{in}$ ]	$11891^{+3686}_{-2473}$	193.93/165	14.41	43.67
			E	0.03 (frz)	$1.16^{+0.14}_{-0.14}$	$0.09^{+0.00}_{-0.00}$ [ $T_{BB}$ ]	1268 (frz)	29.36/42	0.33	
EXO	hard	0160761301	OOE	0.11 (frz)	$1.32^{+0.02}_{-0.02}$	$0.25^{+0.01}_{-0.02}$ [ $T_{in}$ ]	$1041^{+216}_{-181}$	183.23/153	14.59	42.91
			E	0.03 (frz)	$1.14^{+0.10}_{-0.10}$	$0.13^{+0.00}_{-0.00}$ [ $T_{BB}$ ]	318 (frz)	51.95/66	0.34	
AXJ	soft	0402430301	OOE	$18.64^{+0.19}_{-0.19}$	$2.36^{+0.02}_{-0.02}$	–	–	145.68/105	13.28	6.48
			E	$17.14^{+1.05}_{-0.99}$	$3.36^{+0.17}_{-0.16}$	–	–	100.59/86	2.05	
AXJ	soft	0402430401	OOE	$16.86^{+0.81}_{-0.81}$	$1.65^{+0.16}_{-0.21}$	$1.17^{+0.04}_{-0.04}$ [ $T_{BB}$ ]	8.50 (frz)	157.33/104	14.61	8.12
			E	$19.23^{+1.18}_{-1.11}$	$3.83^{+0.20}_{-0.19}$	–	–	85.80/80	1.80	
AXJ	soft	0724210201	OOE	$20.58^{+0.43}_{-0.46}$	2.25 (frz)	$1.53^{+0.07}_{-0.10}$ [ $T_{BB}$ ]	$1.16^{+0.31}_{-0.32}$	121.33/104	15.03	6.37
			E	$17.83^{+1.27}_{-1.19}$	$3.03^{+0.19}_{-0.19}$	–	–	91.19/77	2.36	
AXJ	soft	0762250301	OOE	$16.35^{+0.88}_{-1.07}$	2.09 (frz)	$1.77^{+0.02}_{-0.02}$ [ $T_{BB}$ ]	$2.98^{+0.45}_{-0.44}$	132.08/105	19.57	8.98
			E	$18.03^{+2.65}_{-2.37}$	$3.33^{+0.48}_{-0.44}$	–	–	42.53/50	2.18	
AXJ	hard	0723410301	OOE	$19.53^{+0.88}_{-0.88}$	$1.82^{+0.08}_{-0.08}$	–	–	103.05/101	2.13	9.68
			E	9.39 (frz)	$2.05^{+0.56}_{-0.55}$	–	–	4.87/8	0.22	
AXJ	hard	0723410401	OOE	$17.15^{+0.84}_{-0.83}$	$1.65^{+0.08}_{-0.08}$	–	–	91.22/102	1.34	10.31
			E	17.15 (frz)	$2.65^{+0.10}_{-0.08}$	–	–	3.63/5	0.13	
AXJ	hard	0723410501	OOE	$19.50^{+1.03}_{-1.01}$	$1.89^{+0.10}_{-0.10}$	–	–	74.65/99	1.43	5.72
			E	19.50 (frz)	$2.39^{+0.52}_{-0.54}$	–	–	10.74/10	0.25	
XTE	soft	0206990401	OOE	$0.27^{+0.01}_{-0.01}$	$1.92^{+0.03}_{-0.02}$	–	–	197.74/150	2.58	129
			E	–	–	–	–	–	0.02	

Table 5: The emission and absorption line parameters of the eclipse and OOE spectra of the three eclipsing LMXBs, MXB: MXB 1659–298, EXO: EXO 0748–676, AXJ: AX J1745.6–2901, XTE: XTE J1710–281, E: Eclipse, OOE: Out-of-eclipse,  $E_{em}$ : Emission line energy (keV),  $w_{em}$ : Emission line width (keV),  $F_{em}$ : Emission line flux (photons  $\text{cm}^{-2} \text{sec}^{-1}$ ), EqW: Equivalent width of emission line (eV),  $E_{ab}$ : Absorption line energy (keV),  $w_{ab}$ : Absorption line width (keV),  $S_{ab}$ : Absorption line strength. Errors in line energies and widths are given with 90% confidence limit, whereas that on emission line flux, equivalent width of the emission line and absorption line strength are given at  $1\sigma$  confidence limit.

Source	State	OB ID	Phase	$E_{em}$	$w_{em}$	$F_{em}$	EqW	$E_{ab}$	$w_{ab}$	$S_{ab}$
MXB	soft	0008620601	OOE	–	–	–	–	$6.89^{+0.11}_{-0.10}$	0.11 (frz)	$0.04^{+0.01}_{-0.01}$
MXB	soft	0008620701	OOE	–	–	–	–	$6.71^{+0.03}_{-0.02}$	0.0064 (frz)	$0.075^{+0.005}_{-0.03}$
			OOE	–	–	–	–	$6.99^{+0.02}_{-0.02}$	0.0077 (frz)	0.073 (frz)
EXO	hard	0160760101	OOE	$0.525$ (frz)	$0.14^{+0.01}_{-0.01}$	$0.01^{+0.001}_{-0.001}$	$58^{+6}_{-6}$	$6.75^{+0.13}_{-0.13}$	0.19 (frz)	$0.02^{+0.01}_{-0.01}$
			E	$1.40^{+0.03}_{-0.03}$	0.000096 (frz)	$0.000017^{+0.000006}_{-0.000006}$	$58^{+20}_{-20}$	–	–	–
			E	$0.89^{+0.01}_{-0.01}$	0.03 (frz)	$0.000093^{+0.000001}_{-0.000001}$	$138^{+15}_{-15}$	–	–	–
			E	$0.51^{+0.02}_{-0.02}$	$0.11^{+0.02}_{-0.02}$	0.00095 (frz)	708	–	–	–
EXO	hard	0160760201	OOE	$0.60^{+0.01}_{-0.01}$	$0.07^{+0.01}_{-0.01}$	$0.004^{+0.001}_{-0.001}$	$42^{+10}_{-10}$	–	–	–
			E	$1.39^{+0.03}_{-0.03}$	0.000015 (frz)	$0.000019^{+0.000005}_{-0.000005}$	$61^{+19}_{-19}$	–	–	–
			E	$1.80^{+0.04}_{-0.03}$	0.0000032 (frz)	$0.000013^{+0.000005}_{-0.000005}$	$72^{+28}_{-28}$	–	–	–
			E	$6.44^{+0.06}_{-0.08}$	0.000062 (frz)	$0.000013^{+0.000005}_{-0.000005}$	$335^{+29}_{-129}$	–	–	–
			E	$0.89^{+0.02}_{-0.01}$	0.03 (frz)	$0.000086^{+0.00001}_{-0.00001}$	$101^{+12}_{-12}$	–	–	–
			E	$0.54^{+0.01}_{-0.02}$	$0.06^{+0.02}_{-0.02}$	$0.00037^{+0.00005}_{-0.00005}$	$201^{+27}_{-27}$	–	–	–
EXO	hard	0160760301	OOE	$0.62^{+0.01}_{-0.01}$	$0.04^{+0.02}_{-0.02}$	$0.002^{+0.0003}_{-0.0003}$	$14^{+2}_{-2}$	–	–	–
			E	$0.55^{+0.02}_{-0.02}$	$0.04^{+0.03}_{-0.04}$	0.00018 (frz)	69	–	–	–
EXO	hard	0160760401	OOE	–	–	–	–	$6.85^{+0.12}_{-0.13}$	0.14 (frz)	$0.013^{+0.004}_{-0.004}$
			E	$0.90^{+0.06}_{-0.03}$	0.000056 (frz)	$0.000037^{+0.000014}_{-0.000013}$	$64^{+24}_{-22}$	–	–	–
EXO	hard	0160760601	OOE	$0.59^{+0.01}_{-0.01}$	$0.05^{+0.01}_{-0.01}$	$0.002^{+0.000}_{-0.000}$	$22^{+0}_{-0}$	6.9 (frz)	$0.18^{+0.13}_{-0.10}$	$0.02^{+0.00}_{-0.00}$
			E	$1.89$ (frz)	$0.11^{+0.09}_{-0.05}$	0.00003 (frz)	236	–	–	–
EXO	hard	0160760801	OOE	$0.58^{+0.01}_{-0.02}$	$0.07^{+0.02}_{-0.01}$	$0.003^{+0.00}_{-0.00}$	$129^{+0}_{-0}$	$6.81^{+0.08}_{-0.08}$	$0.15^{+0.06}_{-0.09}$	$0.02^{+0.00}_{-0.00}$
			E	$1.28^{+0.04}_{-0.05}$	0.06 (frz)	$0.000036^{+0.00001}_{-0.00001}$	$129^{+36}_{-36}$	–	–	–
			E	6.40 (frz)	0.19 (frz)	$0.00003^{+0.000009}_{-0.000009}$	$655^{+196}_{-196}$	–	–	–
			E	$0.595^{+0.02}_{-0.02}$	$0.06^{+0.03}_{-0.02}$	0.00027 (frz)	192	–	–	–
			E	$0.89^{+0.03}_{-0.03}$	$0.07^{+0.03}_{-0.02}$	0.00013 (frz)	262	–	–	–
EXO	hard	0160761301	E	$1.32^{+0.03}_{-0.04}$	0.00016 (frz)	$0.000019^{+0.000006}_{-0.000006}$	$63^{+21}_{-21}$	–	–	–
			E	$0.55^{+0.01}_{-0.01}$	0.002 (frz)	$0.00021^{+0.000036}_{-0.000036}$	$92^{+16}_{-16}$	–	–	–
			E	$0.90^{+0.02}_{-0.02}$	0.03 (frz)	$0.000060^{+0.00001}_{-0.00001}$	$87^{+18}_{-18}$	–	–	–
AXJ	soft	0402430301	OOE	–	–	–	–	$6.68^{+0.03}_{-0.03}$	0.094 (frz)	$0.035^{+0.004}_{-0.003}$
			OOE	–	–	–	–	$6.95^{+0.02}_{-0.02}$	0.02 (frz)	$0.049^{+0.005}_{-0.005}$
AXJ	soft	0402430401	OOE	–	–	–	–	$6.66^{+0.03}_{-0.02}$	0.01 (frz)	$0.03^{+0.01}_{-0.00}$
			OOE	–	–	–	–	$6.96^{+0.01}_{-0.03}$	$0.009^{+0.001}_{-0.001}$	0.15 (frz)
AXJ	soft	0724210201	OOE	–	–	–	–	$6.71^{+0.03}_{-0.03}$	0.004 (frz)	1.03 (frz)
			OOE	–	–	–	–	$6.96^{+0.03}_{-0.01}$	$0.01^{+0.00}_{-0.00}$	0.32 (frz)
AXJ	soft	0762250301	OOE	6.4 (frz)	0.002 (frz)	$0.000042^{+0.00001}_{-0.00001}$	$8^{+2}_{-2}$	$6.71^{+0.04}_{-0.04}$	0.002 (frz)	0.06 (frz)
			OOE	–	–	–	–	$6.96^{+0.02}_{-0.01}$	0.004 (frz)	5.76 (frz)

Table 6: *zxipcf* parameters for the OOE spectra of EXO 0748–676, where  $N_h$ : Line of sight equivalent hydrogen column density associated with model component *zxipcf*,  $\log(\xi)$ : Logarithm of ionization parameter  $\xi$ , CvF: covering fraction. Errors are given with 90% confidence limit.

OB ID	$N_h$ ( $10^{22} \text{ cm}^{-2}$ )	$\log(\xi)$	CvF
0160760101	$5.35^{+0.32}_{-0.24}$	$1.37^{+0.19}_{-0.10}$	$0.76^{+0.03}_{-0.04}$
0160760201	$5.62^{+0.72}_{-0.58}$	$2.02^{+0.03}_{-0.04}$	$0.61^{+0.04}_{-0.04}$
0160760301	$4.18^{+0.47}_{-0.37}$	$2.05^{+0.03}_{-0.03}$	$0.55^{+0.03}_{-0.04}$
0160760401	$2.14^{+0.18}_{-0.17}$	$0.59^{+0.10}_{-0.11}$	$0.92^{+0.03}_{-0.04}$
0160760601	$4.64^{+0.35}_{-0.29}$	$1.97^{+0.02}_{-0.02}$	$0.72^{+0.03}_{-0.03}$
0160760801	$6.35^{+0.56}_{-0.46}$	$1.96^{+0.02}_{-0.02}$	$0.76^{+0.03}_{-0.04}$
01607601301	3.86 (frz)	$1.28^{+0.17}_{-0.18}$	$0.79^{+0.05}_{-0.05}$

Table 7: 0.3-3 keV flux obtained from the best fit eclipse spectra of the three eclipsing LMXBs including the dust scattering model component  $xscat$  ( $F_{low,xs}$ ) and that excluding  $xscat$  ( $F_{low}$ ). Last two columns give the reduced  $\chi^2$  of the best fit eclipse spectra including and excluding the model component  $xscat$  respectively. MXB: MXB 1659–298, EXO: EXO 0748–676, AXJ: AX J1745.6–2901

Source	State	OB ID	$F_{xs}$ (0.3-3 keV) ( $10^{-11}$ ergs $\text{cm}^{-2}$ $\text{s}^{-1}$ )	F (0.3-3 keV) ( $10^{-11}$ ergs $\text{cm}^{-2}$ $\text{s}^{-1}$ )	$\chi^2_{xs}/\text{DOF}$	$\chi^2/\text{DOF}$
MXB	soft	0008620601	1.3285	1.3277	21.75/25 (0.87)	21.76/25 (0.8704)
MXB	soft	0008620701	1.3553	1.3558	103.24/106 (0.9740)	103.04/106 (0.9721)
EXO	hard	0160760101	0.2288	0.2286	67.14/70 (0.9591)	67.12/70 (0.9588)
EXO	hard	0160760201	0.2314	0.2317	56.51/55 (1.0274)	56.52/55 (1.0276)
EXO	hard	0160760301	0.2338	0.2338	97.58/84 (1.1617)	97.46/84 (1.1602)
EXO	hard	0160760401	0.1617	0.1624	46.29/34 (1.3615)	46.25/34 (1.3603)
EXO	hard	0160760601	0.1883	0.1884	37.90/40 (0.9475)	37.78/40 (0.9445)
EXO	hard	0160760801	0.2195	0.2196	29.36/42 (0.6990)	29.31/42 (0.6978)
EXO	hard	0160761301	0.2258	0.2262	51.95/66 (0.7871)	52.28/66 (0.7921)
AXJ	soft	0402430301	0.0742	0.0742	100.59/87 (1.1562)	100.58/87 (1.1561)
AXJ	soft	0402430401	0.0552	0.0557	85.80/80 (1.0725)	85.37/80 (1.0671)
AXJ	soft	0724210201	0.0511	0.0515	91.19/77 (1.1843)	90.45/77 (1.1747)
AXJ	soft	0762250301	0.0569	0.0575	42.53/50 (0.8506)	42.37/50 (0.8474)
AXJ	hard	0723410301	0.0113	0.0115	4.87/8 (0.6087)	4.87/8 (0.6087)
AXJ	hard	0723410401	0.0027	0.0028	3.63/5 (0.726)	3.62/5 (0.724)
AXJ	hard	0723410501	0.0027	0.0028	10.74/10 (1.074)	10.74/10 (1.074)

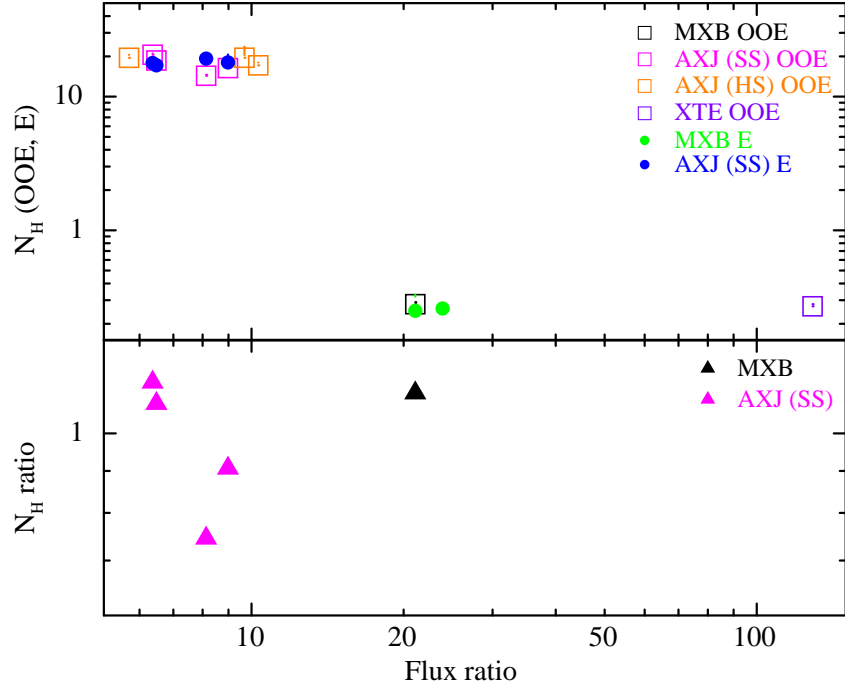


Figure 11:  $N_{\text{H}}$  during OOE and eclipse (top panel) and their ratio (bottom panel) plotted with OOE to eclipse flux ratio for the three eclipsing LMXBs. In the top panel black, pink, orange and purple boxes denote OOE  $N_{\text{H}}$  of MXB 1659–298, AX J1745.6–2901 soft state, AX J1745.6–2901 hard state and XTE J1710–281 observations respectively, whereas green and blue circles represent  $N_{\text{H}}$  during eclipse of MXB 1659–298 and AX J1745.6–2901 soft state observations respectively. The black and pink triangles in the bottom panel represent OOE to eclipse  $N_{\text{H}}$  ratio for MXB 1659–298 and AX J1745.6–2901 soft state observations respectively. The observations for which  $N_{\text{H}}$  could not be constrained are not plotted here.

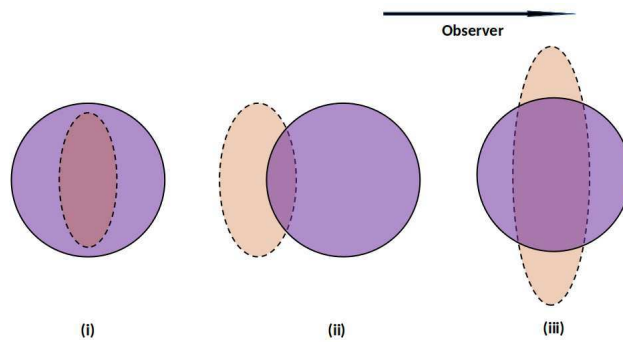
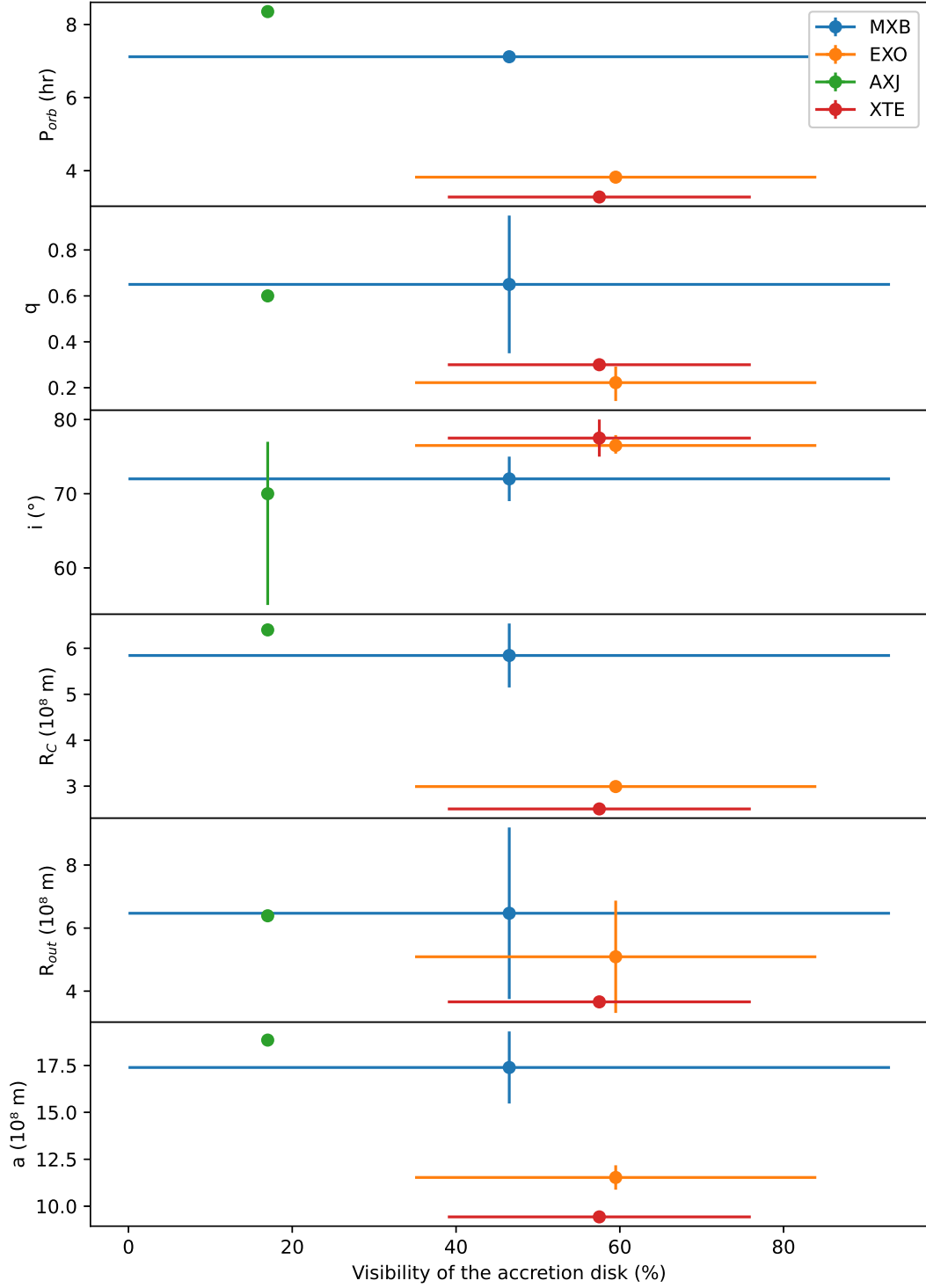


Figure 12: The types of occultation during maximum eclipse phase depending upon the inclination  $i$ , radius of the companion star  $R_{\text{C}}$ , radius of the accretion disk  $R_{\text{out}}$  and the binary separation  $a$ . (i) The projection of the accretion disk (ellipse) is fully covered by the projection of the companion star (circle). (ii) The projection of the accretion disk is partially covered and intersected by the projection of the companion star at two points. (iii) The projection of the accretion disk is partially covered and intersected by the projection of the companion star at four points.



22  
 Figure 13: The orbital parameters, radius of the companion star and accretion disk are plotted against visible (during maximum eclipse phase) portion of the accretion disk with respect to its total area in %.  $P_{orb}$ : orbital period of the binary,  $q$ : ratio of companion star's mass with neutron star's mass,  $i$ : inclination of the system,  $R_C$ : radius of the companion star,  $R_{out}$ : radius of the accretion disk,  $a$ : binary separation.

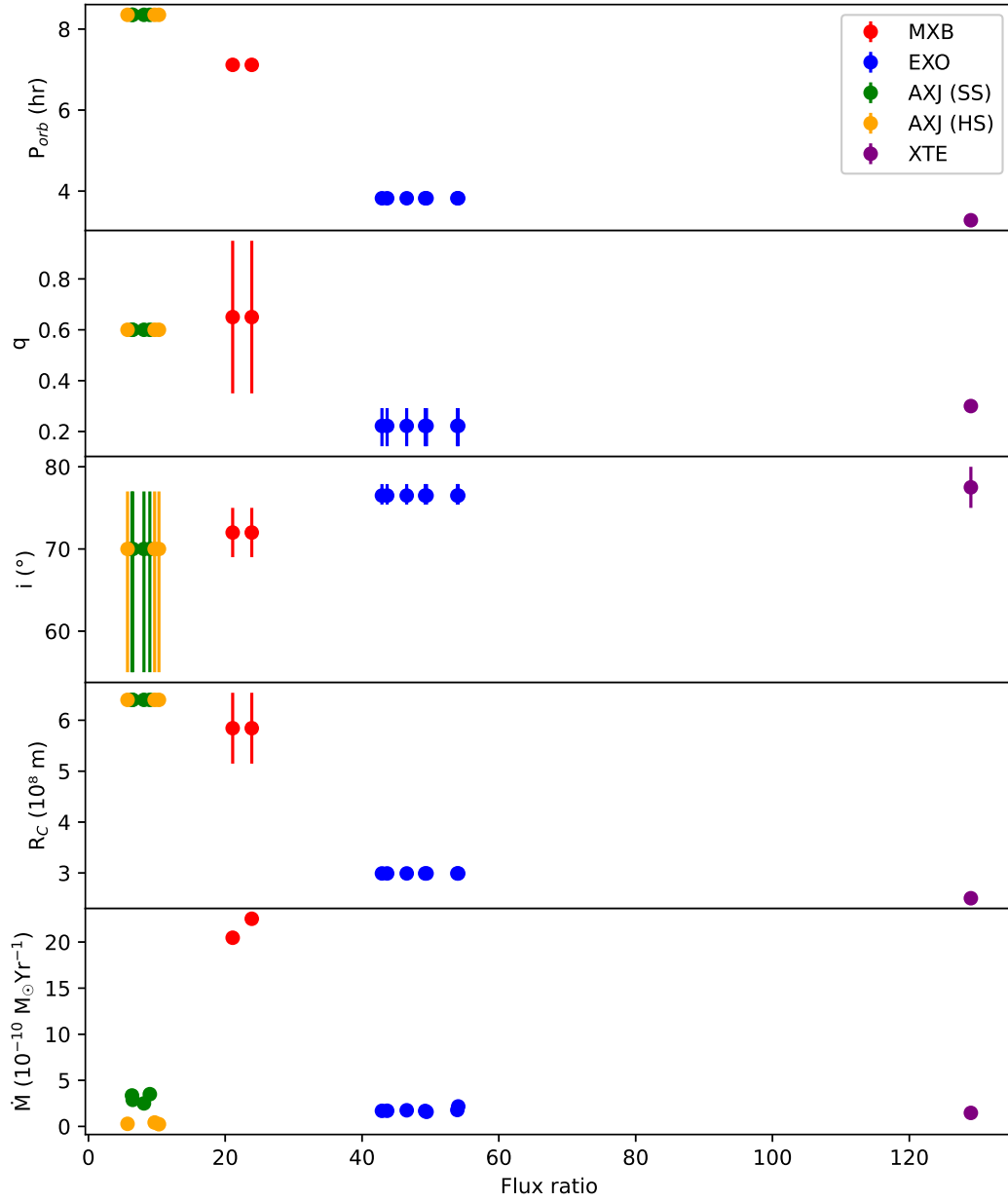


Figure 14: The orbital parameters, radius of the companion and mass accretion rate are plotted against OOE to eclipse flux ratio.  $P_{orb}$ : orbital period of the binary,  $q$ : ratio of companion star's mass with neutron star's mass,  $i$ : inclination of the system,  $R_C$ : radius of the companion star,  $\dot{M}$ : Mass accretion rate.

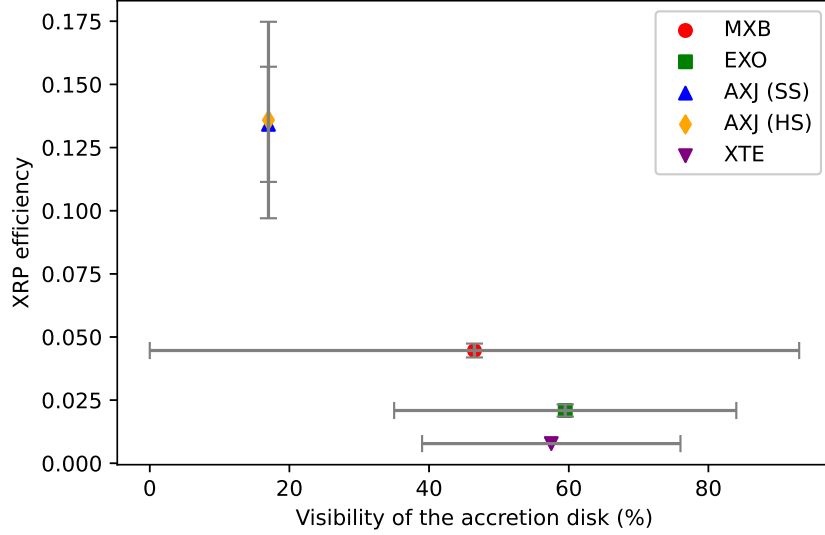


Figure 15: The X-ray reprocessing efficiency (reciprocal of the ratio of OOE flux to eclipse flux) is plotted against visible (during total eclipse) portion of the accretion disk with respect to it's total area in %.

LMXBs the main reprocessing agent is the accretion disk and any structures if present on the disk. Corona above the accretion disk and outflows from disk also act as reprocessing agents in the systems where these are present. In some cases slow and dense wind from the red giant companion (Masetti et al. 2007, Nespoli et al. 2010) acts as a reprocessing agent. During eclipses the continuum is suppressed, because the direct emission from the neutron star is blocked and the emission lines which are often produced in the surrounding medium are expected to be suppressed by a lesser extent (Aftab, Paul and Kretschmar, 2019). The eclipse spectrum is therefore expected to show larger equivalent width and better detectability of the emission lines compared to the OOE spectrum, if the emitting plasma is present in the medium surrounding the central source. Absorption lines in LMXBs are produced during the passage of the photons through the accretion disk atmosphere (Róžańska et al. 2014, Trigo and Boirin 2016). So their detectability is better during OOE phase. However depending upon the extent of the accretion disk; its orientation with respect to the line of sight; structures in the disk; distribution of the material around the compact object and its density, the eclipse spectrum in comparison to the OOE spectrum can be different in different sources and also in the same source at different epochs.

To understand the X-ray reprocessing properties of LMXB systems we have analyzed 17 observations of 4 eclipsing LMXB sources with *XMM-Newton* EPIC pn. These LMXBs have orbital period in the range of 3.281 hour to 8.351 hour, so far known mass of the companion is in the range of  $0.2M_{\odot}$  to  $1.0M_{\odot}$  (EXO 0748–676: Hynes and Jones 2009, AX J1745.6–2901: Maeda et al. 1996 and MXB 1659–298: Ponti et al. 2018). We have compared eclipse spectra of these sources and also compared eclipse and OOE spectra of each observation. We have obtained flux during eclipse and OOE phase in each observation from the best fit models. We have also estimated the flux by fitting each spectrum with a simple powerlaw modified with photoelectric absorption and found the same value of flux that obtained with best fit model. This signifies that the quoted flux are independent of the choice of models. We have measured the X-ray flux of



theses sources during eclipses and have made a comparison with the OOE fluxes. This is to be seen in the context of each binary separately, specially in context with their orbital parameters, for example, size of the binary, relative size of the accretion disk with companion star's, for which the binary parameters of each source is shown Table 1 and 8.

Two observations of MXB 1659–298 observed in soft states show nearly same fluxes in the energy range of (0.3-10) keV in the eclipse phases. Flux ratio of the OOE to eclipse phases are also quite similar, which signifies that X-ray reprocessing properties of the system in the two soft states of the source, observed within a gap of  $\sim 1$  year are consistent.  $N_{\text{H}}$  obtained from the eclipse and OOE spectra of the two observations do not vary much, this signifies nearly consistent environment surrounding the neutron star. Black body temperature found in the two observations in OOE phase are high ( $>1$  keV). Considering the distance of the system to be 10 – 16 kpc (Trigo et al., 2006) and from the blackbody normalization ( $(\frac{R_{\text{km}}}{D_{10\text{kpc}}})^2$ : 2.41 – 14.07, Table 4), the size (radius) of the emitting region is estimated as  $\sim 1.6 - 6$  km. In the composite eclipse (OOE) spectra we see both the eclipse (OOE) spectra almost overlap (Fig 4), that indicates nearly consistent accretion and emission scenario in the system in the two observations, observed with a gap of  $\sim 1$  year.

In EXO 0748–676, continuum of the eclipse spectra drops nearly by same factor throughout the (0.3-10) keV energy range from that of the OOE spectra in all the seven observations (Figure 6). The OOE to eclipse flux ratio has a short range (43-54) in the seven observations. These indicate stability of X-ray reprocessing in the source during these observations. All seven OOE spectra required partial covering absorption by partially ionized material for the best fit. The partially ionized materials cover (55 – 92%) (Table 6) of the source emission. This component was not required to fit the eclipse spectra, which indicates that these ionized materials are either close to the source and / or distributed in a narrow region, and fully blocked during eclipse. A weak blackbody emission ( $T_{\text{BB}}$ : 0.09-0.21 keV) has been observed (with component *bbdyrad*) during eclipse i.e. from a region at least at a distance equal to the radius of the companion from the neutron star. The size (radius) of these emitting regions are estimated to be 5-16 km using the blackbody normalization ( $(\frac{R_{\text{km}}}{D_{10\text{kpc}}})^2$ : 123 – 325, Table 4) and distance of the source ( $5.8 \pm 0.9$  to  $7.7 \pm 0.9$  kpc, Wolff et al. 2005). Also a weak black body emission ( $T_{\text{in}}$ : 0.09-0.25 keV) from the disk is observed (with model component *diskbb*) during OOE phase of all the seven observations. The apparent inner accretion disk radius is estimated to be 320 – 3336 km, from the the disk normalization ( $(\frac{R_{\text{in}}}{D_{10}})^2 \cos\theta$ : 860 – 23181, Table 4), distance to the source and inclination angle ( $(5-11)$  kpc, Trigo et al. 2006;  $76.5^{+1.4}_{-1.1}$ , Knight et al. 2022) of the source. A high temperature blackbody emission ( $T_{\text{BB}}$ :  $\sim 4$  keV) is observed in one observation (OB ID: 0160760101) during OOE phase. The size (radius) of this blackbody emitting region is estimated to be (0.68 – 2.58 km), from the normalization ( $0.08^{+0.03}_{-0.03}$ ) and distance to the source.

1 – 5 emission lines have been observed during eclipse phase of the seven observations of EXO 0748–676 (details are given in Table 5). The origin of 0.5 keV, 0.89 keV, 1.28 keV, 1.32 keV, 1.4 keV, 1.8 keV and 1.89 keV emission lines are possibly from O  $K_{\alpha 1}$ , Ne  $K_{\alpha 1}$ , Mg  $K_{\alpha 1}$ , Mg  $K_{\beta}$ , Al  $K_{\alpha 1}$ , Si  $K_{\alpha 1}$ , Si  $K_{\beta}$  respectively.  $\sim 0.6$  keV,  $\sim 0.9$  keV and  $\sim 1.39$  keV emission lines possibly are blend of other higher ionised emission lines with O  $K_{\alpha 1}$ , Ne  $K_{\alpha 1}$  and Mg  $K_{\beta}$  respectively. Detection of these lines in the eclipse phase indicates distribution of ionised Oxygen, Magnesium, Aluminium, Silicon in the extended medium surrounding the neutron star, which is at least at a distance equal to the radius of the companion from the neutron star. Emitting plasma consisting these ions may be present in the outer accretion disk or in the extended corona. Presence of  $\sim 0.5$  keV emission line during OOE phase in five observations indicates presence of ionised

Oxygen close to the neutron star. Fe XXV / Fe XXVI absorption lines have been detected during OOE phase in three observations (OB ID: 0160760401, 0160760601, 0160760801), these indicate that most of the photo-ionized absorbing plasma is located near the compact object. Presence of extended corona have been proposed by Jimenez et al. (2002). In persistent spectra of EXO 0748–676 with EPIC pn, Trigo et al. (2006) have found emission lines of O VII and Ne IX. Cottam et al. (2008) have observed Fe XXV, XXVI (n=2-3) and O VIII (n=1-2) absorption lines and emission lines from Neon, Nitrogen, Oxygen ions during bursts in EXO 0748–676 with *XMM-Newton* RGS. They propose photosphere of the neutron star as the origin of the absorption features and the emission lines possibly originate in the extended structure to the outer atmosphere. Psaradaki et al. (2018), with *XMM-Newton* RGS detected several lines from ionized Neon, Nitrogen and Oxygen during eclipses. They confirm an extended atmosphere above the accretion disk.

The composite eclipse spectra for the seven observations of this source almost overlap (top left panel of Figure 6), this indicates nearly consistent spectra and reprocessed X-ray flux in eclipses during two months of observation period. This also indicates similar kind of distribution of matter in the outer accretion disk and in the surrounding region, as during eclipse inner accretion disk is blocked by the companion. Composite OOE spectra obtained including the dips intervals of the seven observations show an overlap above  $\sim 4$  keV while there is significant variation in the spectrum below 4 keV (top right panel of Figure 6). The variation in the low energy part of the spectrum is likely to be due to the variable patterns in the inner accretion disk causing dips in EXO 0748–676 (Raman et al., 2017). The vertical structures that cause the dips in low energy X-rays, possibly vary in structure and density in a manner, that they cause variation in the reprocessing of lower energy X-ray photons, whereas higher energy X-rays are almost unaffected by these structures. The composite OOE spectra obtained excluding the dips intervals shows an overlap  $\geq 2$  keV (bottom panel). The variation  $\leq 2$  keV in the OOE spectra obtained excluding the dips intervals indicates some other structures/irregularities on the inner accretion disk other than the vertical structures that causes variation below 4 keV. Variation of soft X-rays could also be due to different accreting bulges produced at the impact point between outer accretion disk and the accretion stream (Raman et al., 2017).

In AX J1745.6–2901, the line of sight equivalent Hydrogen column density ( $N_H$ ) found in both soft and hard state observations during eclipse and OOE phases are comparable, that indicates nearly consistent environment in the system in both soft or hard states, during the period of the seven observations.  $N_H$  found during OOE and eclipse phase in AX J1745.6–2901 is nearly two orders of magnitude higher compared to that found in other eclipsing sources analysed in this text (Table 4). This indicates that the medium surrounding the neutron star in this source is more dense compared to other three sources. The photon index of the eclipse spectrum is higher than that of the OOE spectrum in both the spectral states in AX J1745.6–2901, this indicates that the photons received during eclipses are not produced from pure reflection of the primary source photons. We need a systematic analysis of OOE and eclipse spectra of the source with a large number of data sets to find out the exact cause of this behaviour.

Like MXB 1659–298, He like Fe XXV and H like Fe XXVI absorption line have been detected in the OOE phase in all the soft state observations of AX J1745.6–2901, which indicates hot, ionized material close to the neutron star during soft state. No spectral line has been observed during OOE phase in the hard state. Ponti et al. 2015, Ponti et al. 2017 have observed Fe K absorption features in the soft state with *XMM-Newton* (*XMM-Newton* and *NuSTAR*), but these features were not seen in the hard states spectra they have analyzed. Their (Ponti et al., 2015) analysis show the variability due to change in the ionizing continuum, so they rule out over

ionization as the reason for the disappearance of these absorption lines during hard state. They suggest that this behaviour could be due to the change of physical properties of plasma with the change of spectral energy distribution between the soft and hard state of the source. Hyodo et al. (2009), had also found the same features in the soft state of the source with *Suzaku*. The disk corona could be the origin of these absorption features (Hyodo et al. 2009, Ponti et al. 2015). Ponti et al. (2018) have obtained highly variable absorption in the soft states in the *XMM-Newton* spectra while all the hard state spectra with *XMM-Newton* and *NuSTAR* were well fitted with constant column density of neutral absorption. They suggest that the neutral absorption is mostly from the ISM.

We have observed high blackbody temperature ( $> 1$  keV) in the three soft state observations of AX J1745.6–2901 during OOE phase. From the normalization ( $(\frac{R_{\text{km}}}{D_{10\text{kpc}}})^2$ : 0.84–3.43, Table 4) and distance to the source (8.3 kpc, Genzel et al. 2010, Bland et al. 2016, Gillessen et al. 2017), the size (radius) of the emitting regions is estimated to be 0.8-1.5 km. In the soft-state below  $\sim 3$  keV the intensities in the eclipse and the OOE spectra differ by a lower factor ( $\sim 3$ -5), than the intensities above  $\sim 3$  keV (rightmost figure of Figure 7). But the hard state spectra (rightmost figure of Figure 8) show that below 3 keV, there is negligible number of photons received during eclipse. These possibly indicates that the outer accretion disk is blocked during eclipses, as most of the lower energy X-ray emission comes from the outer accretion disk, which is not observed. Soft-state composite OOE spectra of the system show nearly comparable intensity for the three observations, while intensity for the other observations is nearly more than 5 times lower than these three spectra (right figure of Figure 9). In the reprocessed eclipse spectra also, the intensity of this soft state observation goes down by similar factor compared to the other three soft state observations (left figure of Figure 9). These indicate nearly steady structure of the accretion disk, during these soft-state observations. OOE to eclipse flux ratio is comparable in the soft and hard states (Table 4), which indicates X-ray reprocessing property of the matter surrounding the compact object is independent of the spectral state of the source.

EPIC pn eclipse spectrum of XTE J1710–281 has very poor statistics and the flux is very low during this observation. The exposure time is 367 seconds for this observation, while the source has an eclipse duration of 420 seconds (Jain and Paul, 2011). With much less exposure time (98 seconds) we have observed more number of photons in one eclipse observation of MXB 1659–298 (OB ID: 0008620601). The outer accretion disk radius in this system is found to be larger than the radius of the companion ( $R_{\text{out}} > R_{\text{C}}$ ). The large OOE to eclipse flux ratio ( $\sim 129$ ) for this source perhaps indicates lower scale height of the accretion disk in this source. Because when the scale height is low, the solid angle covered by the outer accretion disk to the central source is low, which perhaps causes lesser reprocessing.

To understand the types of occultation in the LMXB systems during maximum eclipse phase (when the occultation is maximum in the whole eclipse phase) depending upon the binary separation  $a$ , radius of the companion  $R_{\text{C}}$ , radius of the disk  $R_{\text{out}}$  and the inclination  $i$  of the system we have sketched three possibilities, which are given in Figure 12. The values of  $R_{\text{C}}$ ,  $R_{\text{out}}$  and  $a$  are listed in Table 8. The projection of the circular accretion disk of radius  $R_{\text{out}}$  on the sky plane (the plane perpendicular to the line of sight) is an ellipse of semi major axis length  $R_{\text{out}}$  and semi minor axis length  $R_{\text{out}}\cos(i)$ . The projection of spherical companion star of radius  $R_{\text{C}}$  on the sky plane is a circle of radius  $R_{\text{C}}$ . The projection of the companion star may fully cover the projection of the accretion disk, or partially cover the projection of the accretion disk with two or four intersections (left, middle, right figure respectively in Figure 12). The four point intersection is given in Court et al. (2019). Assuming a small tilt of the accretion disk with the orbital plane (as the tilt is not known accurately) and no wrap in the disk, we have derived the occulted area

Table 8: List of radius of the companion star  $R_C$ , radius of the accretion disk  $R_{out}$  and the orbital separation  $a$  respectively for the four LMXB systems.

Source	$R_C$ ( $10^8$ m)	$R_{out}$ ( $10^8$ m)	$a$ ( $10^8$ m)
MXB 1659–298	(5.15-6.54) <sup>a2</sup>	(3.75-9.19) <sup>◊</sup>	(15.47-19.31) <sup>*</sup>
EXO 0748–676	2.992 <sup>b2</sup>	(3.31-6.87) <sup>◊</sup>	(10.88-12.18) <sup>*</sup>
AX J1745.6–2901	6.40 <sup>*</sup>	6.39 <sup>◊</sup>	18.85 <sup>*</sup>
XTE J1710–281	2.51 <sup>*</sup>	3.66 <sup>◊</sup>	9.43 <sup>*</sup>

<sup>a2</sup>(Iaria et al., 2018), <sup>b2</sup>(Knight et al., 2022)

<sup>\*</sup> Derived from orbital period ( $\frac{R_C}{R_\odot} \sim 0.11P_{orb}$ , Frank, King and Raine 2002)

<sup>◊</sup> Estimated using the relation  $R_{out} \sim 0.8 \times R_{LNS}$ , where  $R_{LNS}$  is the Roche lobe radius of the neutron star, details are given in section 1.

<sup>\*</sup> Calculated using Kepler's third law, as mentioned in section 1)

of the projection of the accretion disk on the sky plane by the projection of the companion star during maximum eclipse phase. In the first case (when the accretion disk is fully covered by the companion star) the occulted area is the full area of the ellipse on the sky plane. In the other two cases first we obtained the intersection points by solving equations of ellipse and circle. Then integrating over the overlapping area of the ellipse and the circle between the intersection points we obtained the total occulted area of the disk. The details of the derivations of the occulted and hence visible area of the accretion disk are given in the Supplementary Materials in Section 5.

To understand the variation of the visibility of the accretion disk as functions of orbital parameters and the radius of the companion and the accretion disk, in Figure 13 we have plotted these parameters against the percentage of the accretion disk that is visible during total eclipse. The expression for the visibility of the accretion disk (%) can be found in the Supplementary Materials in section 5. It is obtained by dividing the visible area of the disk by total area of the disk multiplied by 100. It is a function of the inclination of the system  $i$ , radius of the disk  $R_{out}$  and radius of the companion star  $R_C$  and binary separation  $a$ . As the binary separation  $a$  and the orbital period  $P_{orb}$  is correlated (the first equation given in section 1), the visibility is also a function of  $P_{orb}$ . Mass ratio  $q$  between the companion and the neutron star and binary separation  $a$  are also correlated (3rd equation of section 1), so the visibility of the disk is also a function of  $q$ . The variation of visibility with  $a$  and  $P_{orb}$  are similar, which is in conciliation with equation 1. We see high anti-correlation between the visibility of the disk and both  $a$  and  $P_{orb}$  with correlation coefficient ( $r$ ) of -0.84 and -0.89 respectively (with the visibility).  $R_C$  is also highly anticorrelated with the visibility with  $r = -0.85$ .  $q$  and  $R_{out}$  are moderately anticorrelated with the visibility with  $r$  of -0.72 and -0.67 respectively. A positive correlation is found between the inclination  $i$  and the visibility of the disk with  $r = 0.90$  and  $R^2$  (goodness of fit) = 0.80. The occultation is observed to be more when  $i \sim 70^\circ$  compared to the case when  $i$  is  $\sim 80^\circ$ .

To understand the XRP efficiency (reciprocal of OOE to eclipse flux) as functions of binary characteristics, we have plotted the orbital parameters ( $P_{orb}$ ,  $q$ ,  $i$ ,  $a$ ), radius of the companion  $R_C$  and mass accretion rate  $\dot{M}$  with the variation of OOE to eclipse flux ratio in Figure 14. To estimate  $\dot{M}$  we have obtained total unabsorbed flux ( $F$ ) in 3-10 keV energy range for each observation during OOE phase (using CFLUX command in XSPEC) and used the expression  $\eta \times d\dot{M}/dt \times c^2 = F \times 4\pi d^2$ , where  $\eta$  is the mass to energy conversion efficiency in a neutron star (0.15, Frank, King and Raine 2002),  $c$  is speed of light in free space and  $d$  is the distance to the

source.  $P_{\text{orb}}$  and  $R_C$  are observed to be highly anticorrelated with the OOE to eclipse flux ratio with  $r$  of -0.83 and -0.83 respectively (with the flux ratio).  $q$  is moderately anticorrelated with the OOE to eclipse flux ratio with  $r = -0.71$ .  $i$  is highly correlated with the flux ratio with  $r = 0.83$ . Very weak anti-correlation is seen between the mass accretion rate  $\dot{M}$  and the flux ratio with  $r = -0.15$ .

In Figure 15 we have plotted the XRP efficiency with the percentage of the projected disk area that is visible during maximum eclipse phase (visibility of the disk in %). A correlation is expected between the X-ray reprocessing efficiency and the visible area of the accretion disk during maximum eclipse. But this is not observed, rather a negative relation is observed with  $r = -0.99$  and  $R^2 = 0.99$ . The reason of which is not clear from this small sample size and with large uncertainties.

The uncertainties in the orbital parameters lead to the uncertainties in the estimated parameters and hence to the visibility of the disk. We need a large sample and more accurate orbital parameters to find out the exact relationship between the orbital parameters (and also the estimated parameters), the visibility of the disk and the X-ray reprocessing efficiencies of the eclipsing systems.

The system to system differences and unexpected relations between few system parameters with the X-ray reprocessing efficiencies indicate that the X-ray reprocessing characteristics are very sensitive to the detailed geometries of the systems, some of which (scale height of the accretion disk, tilt angle of the accretion disk with respect to the binary orbit/line of sight etc.) are not accurately measurable till date.

### 3.1. SUMMARY

We summarize the results as follows: Flux ratio of the eclipse to OOE spectra shows a range from  $\sim 6$  (in AX J1745.6–2901, OB ID: 0723410501) to  $\sim 129$  (in XTE J1710–281, OB ID: 0206990401), which differs by a factor of  $\sim 21$ . This flux ratio is nearly same in both soft and hard states in AX J1745.6–2901. No spectral line has been found in AX J1745.6–2901 in any of the phase during hard states. Three sources (MXB 1659–298, EXO 0748–676, AX J1745.6–2901 in soft state) show absorption lines during OOE phases. 1-5 emission lines have been observed during eclipse phase of the seven observations of EXO 0748–676. Line of sight equivalent Hydrogen column density is found to be much higher in AX J1745.6–2901 compared to other sources. During out-of-eclipse, in EXO 0748–676, the compact object is found to be partially covered by partially ionized material by at least 55 %. Comparison of this various aspects of the X-ray reprocessing suggests significant differences in the X-ray reprocessing in these LMXBs. The differences could be due to differences in the scale height of the accretion disk, relative size of the accretion disk with respect to the companion, binary separation, mass ratio between the neutron star and the companion, mass accretion rate extension of the accretion disk atmosphere/wind, composition of the scattering agents, their density, ionization level, distribution etc. in these LMXBs, despite all being dipping and eclipsing.

### 3.2. COMPARISON OF X-RAY REPROCESSING BETWEEN HMXB AND LMXB SYSTEMS

In case of HMXBs we have seen much wider variation in the OOE to eclipse flux ratio ( $\sim 8$ -237), which is perhaps due to differences in the stellar wind mass loss properties of the HMXB companions (Aftab, Paul and Kretschmar, 2019). In seven observations of AX J1745.6–2901 and EXO 0748–676, the OOE to eclipse flux ratio have been found to have a narrow range, ( $\sim 6$ -10) and ( $\sim 43$ -54) respectively. Two observations of MXB 1659–298 also show similar

OOE to eclipse flux ratio (21-24). These indicate less variable environment surrounding disk-fed systems. These flux ratios are smaller factor compared to wind accreting supergiant HMXBs (Aftab, Paul and Kretschmar, 2019), where we have seen large variation even in the same source (as much as a factor of  $\sim 3$  in LMC X-4) within a period of less than a year. The smaller value of the OOE to eclipse flux ratio observed in LMXBs indicates greater reprocessing in LMXBs, even though the medium of LMXBs are less dense and less extended compared to that in HMXBs. In the eclipse spectra of HMXBs, 6.4 keV Fe emission line was very common, whereas this line is hardly seen in the eclipse spectra of the LMXBs. These are important outcomes of the two work: X-ray reprocessing in HMXBs and LMXBs. Further analysis of a large number of data sets from HMXB and LMXB systems can get us clear picture about the X-ray reprocessing efficiency and its dependencies in the two types of systems.

#### **4. Conclusion**

- Despite all the sources being dipping and eclipsing, comparison of various aspects of the X-ray reprocessing suggests significant differences in the X-ray reprocessing in these LMXBs, which could be due to differences in the inclination angle, scale height of the accretion disk, relative size of the accretion disk with respect to the companion, binary separation, mass ratio between the neutron star and the companion, mass accretion rate, composition of the scattering agents, their density, ionization level, distribution etc.
- This study presents, for the first time, the derivation of the occulted area of the accretion disk by the companion star (and consequently, the visible area of the disk) for various obscuration geometries during the maximum eclipse phase.
- The eclipse spectra for some of the LMXB sources are being reported for the first time.
- The primary X-ray source and the eclipse spectrum remains nearly same over two months in EXO 0748-676. Different types of vertical structures on the accretion disk produce variation in the lower energy X-rays in the OOE spectrum.
- OOE to eclipse flux ratio are observed to be comparable, irrespective of the intensity state in AX J1745.6-2901.
- Large OOE to eclipse flux ratio and hence low X-ray reprocessing efficiency in XTE J1710-281 indicates low scale height in this system.
- Despite less extended and less dense environment in LMXBs compared to HMXBs, more X-ray reprocessing is observed in the LMXBs.
- Most contrasting outcome with respect to the HMXBs is the lack of strong 6.4 keV line in the eclipse spectrum of LMXBs.

#### **ACKNOWLEDGEMENT**

The data used for this work has been obtained through the High Energy Astrophysics Science

Archive (HEASARC) On- line Service provided by NASA/GSFC. We thank Dr. Wasim Aftab for his help to automate the *XMM-Newton* EPIC-pn script and Anisa Aftab for her co-operation in solving different technical issues during this work. NA would like to thank Dr. Pragati Pradhan and Dr. Gayathri Raman for the constructive discussions related to pn data analysis. NA would like to express sincere thanks to Dr. Dhruv Pathak for the valuable discussions on the theoretical facet of eclipsing systems.

## 5. Supplementary Materials

In section 3, we have seen that depending upon Radius of the accretion disk  $R_{out}$ , radius of the companion  $R_C$ , binary separation  $a$  and inclination  $i$  three scenario can happen during maximum eclipse phase. Figure 12 describes the three scenario. In the first case occulted disk area is 100%, so the visible area of the disk is 0%. Below we show the derivations of the occulted area and hence visible area of the disk during maximum eclipse phase in terms of the above parameters.

### (i) Derivation of the occulted and hence the visible area of the projection of the accretion disk during maximum eclipse phase, when the projection of the companion intersects the projected disk at two points:

In Figure 16 we see the projection of the accretion disk on the sky plane is intersected by the projection of the companion star at two points (P and Q). The inclination of the system is  $i$ , i.e. normal to the orbit of the binary makes an angle  $i$  with the line of sight (LOS). The projection of the circular accretion disk of radius  $R_{out}$  on the sky plane (the plane perpendicular to the LOS) is an ellipse of semi-major axis  $R_{out}$  and semi-minor axis  $R_{out}\cos(i)$ . The projection of the spherical companion of radius  $R_C$  on the sky plane is a circle of radius  $R_C$ . The centre of the projected ellipse and the circle are respectively O and  $O_1$  on the sky plane. We have chosen the origin at O. The X axis is along the line joining O and  $O_1$ .  $OO_1 = a\cos(i)$ , as  $a$  is the binary separation. The whole occulted area is the area enclosed within circular arc PIQ and elliptic arc PTQ. The circular arc PI makes an angle  $\alpha$  at  $O_1$ . The X axis divides this area symmetrically into two halves (enclosed within PITP and QTIQ). So the total occulted area is double the area within PITP. This area is the sum of the area enclosed by circular arc PI, straight line IS, SP (within PISP) and the area enclosed by elliptic arc PT, straight lines TS and SP (within PSTP). These two areas (say  $A_c$  and  $A_{el}$  respectively) are shown in Figure 16 with hollow circles and vertical bars respectively.

The area  $A_c$  can be obtained by subtracting the area of the triangle  $PSO_1$  (say  $A_4$ ) from the area of the circular arc PI made at its centre  $O_1$  (say  $A_3$ ), i.e.  $A_c = A_3 - A_4$ . Solving the equation of the circle  $((x_1 - a\cos(i))^2 + y^2 = R_C^2$  [Eq. 1]) and the ellipse  $(x^2/a_{mj}^2 + y^2/a_{mn}^2 = 1$  [Eq. 2]) we obtained the abscissa ( $x_1$ ) of point P ( $x_1, y_1$ ). where The semi major axis length of the ellipse =  $a_{mj} = R_{out}$  and the semi minor axis length of the ellipse =  $a_{mn} = R_{out}\cos(i)$ .

$y_1 = R_C \sin \alpha$  (from Figure 16)

$$x_1 = \frac{-2a\cos i + \sqrt{4a^2\cos^2 i - 4\tan^2 i(R_C^2 - R_{out}^2 - a^2\cos^2 i)}}{2\tan^2 i} \quad (\text{solving Eq. 1 and Eq. 2})$$

From the equation of the circle (Eq. 1) with  $x = x_1, y = y_1 = R_C \sin \alpha$  we get  $\alpha = \sin^{-1} \frac{\sqrt{R_C^2 - (x_1 - a\cos(i))^2}}{R_C}$

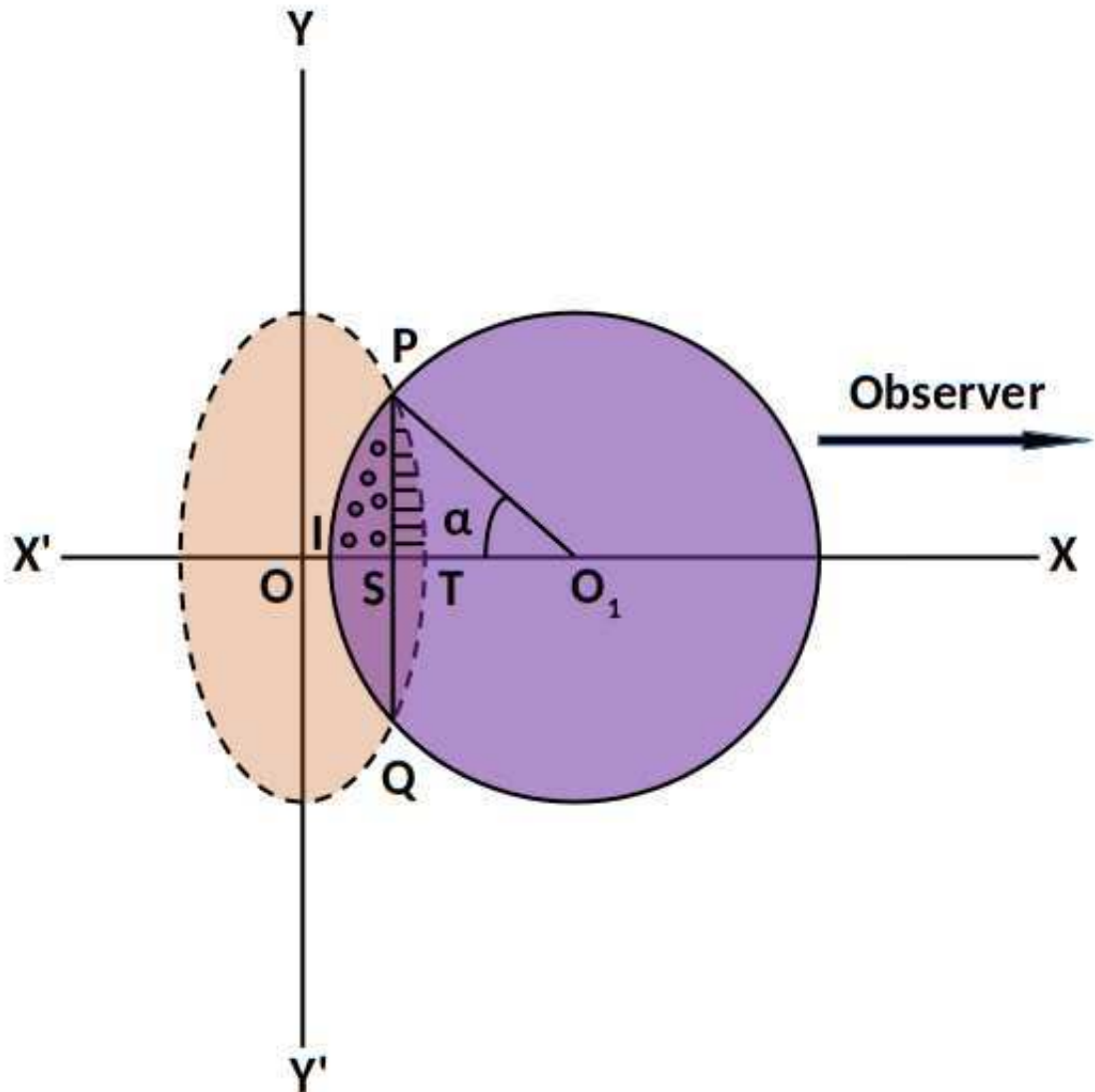


Figure 16: The projection of the accretion disk on the sky plane (ellipse) is intersected by the projection of the companion star at two points (P and Q). O and O<sub>1</sub> are the centers of the ellipse and the circle respectively. The circle and the ellipse intersect the X axis at I and T respectively. The occulted area of the accretion disk is the area covered within PIQTP. The area within PITP is symmetrical to the area covered by QITQ. Hence the total occulted area (within PIQTP) is double the area covered by PITP. The area within PISP (shown with small hollow circles) is the area covered by the circular arc PI and the straight lines IS and SP. The area within PSTP (shown with small vertical bars) is the area covered by the elliptic arc PT and the straight lines ST and SP. The visible area of the accretion disk is obtained subtracting the occulted area from the total area of the ellipse. The derivation of the occulted area and hence the visible area given in section 5.



$$A_3 = \frac{1}{2}R_C^2\alpha \text{ (from Figure 16)}$$

$$A_4 = \frac{1}{4}R_C^2 \sin 2\alpha \text{ (from Figure 16)}$$

$$\text{Hence, } A_c = A_3 - A_4 = \frac{1}{4}R_C^2(2\alpha - \sin 2\alpha)$$

$$A_{el} = \int_{x_S}^{x_T} y dx, \text{ where } x_S = x_1 \text{ and } x_T = R_{out} \cos(i)$$

$$A_{el} = a_{mn} \int_{x_1}^{R_{out} \cos(i)} \sqrt{\left(1 - \frac{x^2}{a_{mj}^2}\right)} dx$$

$$\text{Integrating we get, } A_{el} = \frac{R_{out}^2 \cos(i)}{4}(\pi - 2\theta - \sin 2\theta), \text{ where } \theta = \sin^{-1} \frac{x_1}{R_{out} \cos(i)}$$

$$\text{Hence, the total occulted area of the accretion disk (} A_{occult,2p}) = 2(A_c + A_{el})$$

$$\text{The area of the accretion disk} = A_{disk} = \pi a_{mj} a_{mn} = \pi R_{out}^2 \cos(i)$$

$$\text{The visible area of the accretion disk} = A_{visible,2p} = A_{disk} - A_{occult,2p}$$

$$\text{The percentage of the area of the accretion disk visible during total eclipse} = A_{visible,2p} (\%) = (A_{visible,2p}/A_{disk}) \times 100\%$$

**(i) The derivation of the occulted area of the projection of the accretion disk during total eclipse when the projection of the companion intersects it at four points:**

Figure 17 shows that the projection of the accretion disk on the sky plane is intersected by the projection of the companion star at four points (A, B, A', B'). The description of the geometry remains same as Figure 16. The occulted area of the projection of the accretion disk is the area enclosed within the circular arcs AB, A'B' and elliptic arcs AA', BB'. The line joining O and O<sub>1</sub> i.e. the X axis divides this area symmetrically into two halves (area within ABD'C'A and A'B'D'C'A'). The area enclosed by the circular arc AB and the straight lines BD, DC and CA are shown with hollow circles (within ABDCA, say A<sub>C1</sub>). The area enclosed by the elliptic arc C'A, straight lines AC, CC' (within AC'CA, say A<sub>e11</sub>) and that within elliptic arc BD', straight lines D'D, DB (within D'BDD', say A<sub>e12</sub>) are shown with vertical bars. Solving the equation of the circle (Eq. 1) and the ellipse (Eq. 2) we obtain the abscissas (x<sub>2</sub>, x<sub>3</sub>) of the point A (x<sub>2</sub>, y<sub>2</sub>) and B (x<sub>3</sub>, y<sub>3</sub>).

$$x_3, x_2 = \frac{-2a \cos i \pm \sqrt{4a^2 \cos^2 i - 4 \tan^2 i (R_C^2 - R_{out}^2 - a^2 \cos^2 i)}}{2 \tan^2 i}$$

$$A_{e11} = \int_{x_{C'}}^{x_C} y dx, \text{ where } x_{C'} = -R_{out} \cos(i), x_C = x_2$$

$$A_{e11} = a_{mn} \int_{-R_{out} \cos(i)}^{x_2} \sqrt{\left(1 - \frac{x^2}{a_{mj}^2}\right)} dx$$

Deriving the above integration we get,

$$A_{e11} = \frac{R_{out}^2 \cos(i)}{4}(\pi + 2\theta_2 + \sin 2\theta_2) \text{ where } \theta_2 = \sin^{-1} \frac{x_2}{R_{out} \cos(i)}$$

$$A_{e12} = \int_{x_D}^{x_{D'}} y dx, \text{ where } x_D = x_3 \text{ and } x_{D'} = R_{out} \cos(i)$$

$$A_{e12} = a_{mn} \int_{x_3}^{R_{out} \cos(i)} \sqrt{\left(1 - \frac{x^2}{a_{mj}^2}\right)} dx$$

$$A_{e12} = \frac{R_{out}^2 \cos(i)}{4}(\pi - 2\theta_3 - \sin 2\theta_3) \text{ where } \theta_3 = \sin^{-1} \frac{x_3}{R_{out} \cos(i)}$$

$$A_{C1} = \int_{x_C}^{x_D} y dx, \text{ where } x_C = x_2 \text{ and } x_D = x_3$$

$$A_{C1} = \int_{x_2}^{x_3} \sqrt{R_C^2 - (x - a \cos(i))^2} dx$$

Deriving the above integration we get,

$$A_{C1} = \frac{R_C^2}{4} [2(\theta_{max} - \theta_{min}) + \sin 2\theta_{max} - \sin 2\theta_{min}]$$

$$\text{where } \theta_{max} = \sin^{-1} \frac{x_3 - a \cos(i)}{R_C} \text{ and } \theta_{min} = \sin^{-1} \frac{x_2 - a \cos(i)}{R_C}$$

$$\text{Hence, the total occulted area of the accretion disk (} A_{occult,4p}) = 2(A_{e11} + A_{e12} + A_{C1})$$

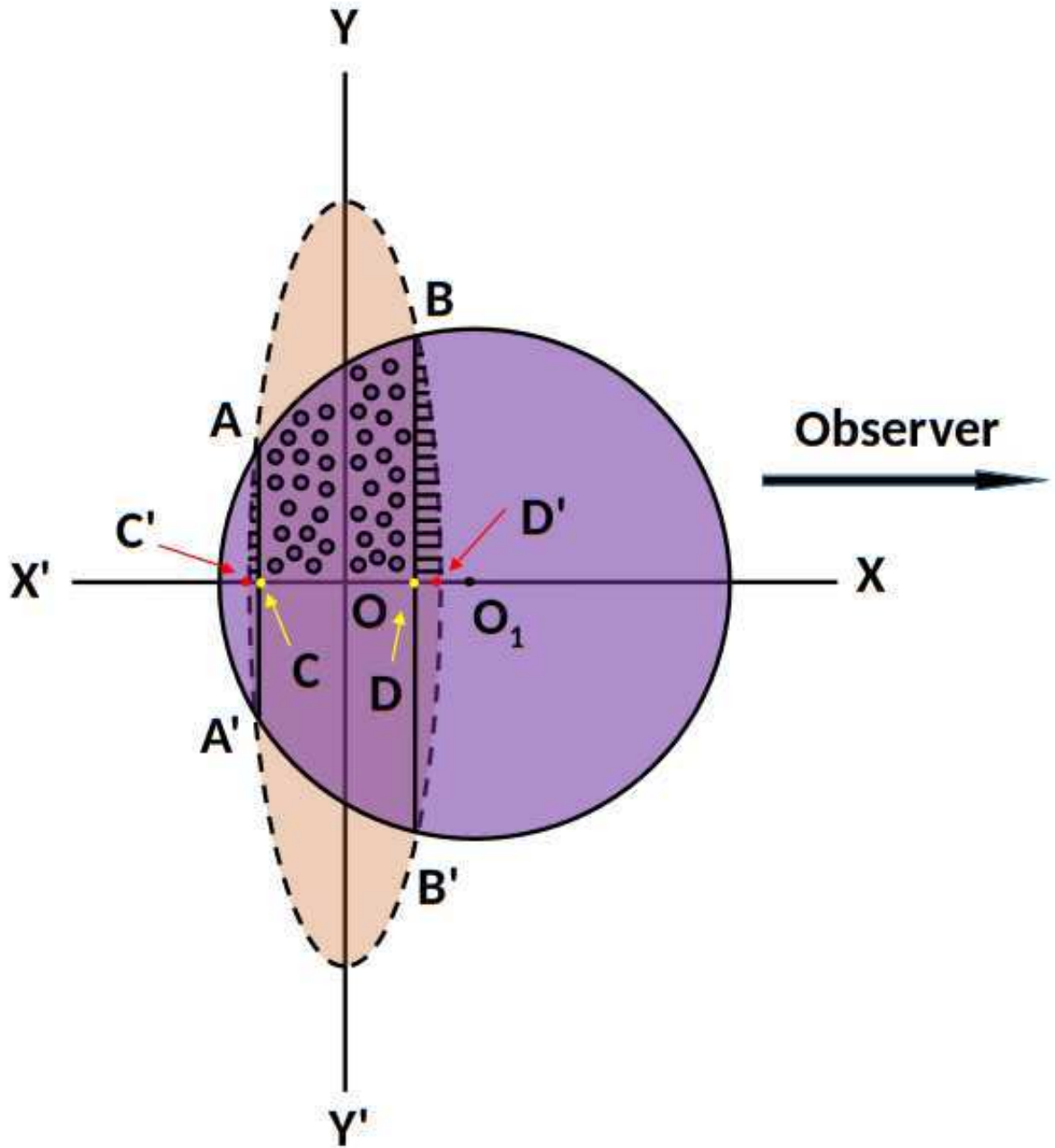


Figure 17: Similar to Figure 16. Here the projection of the accretion disk on the sky plane (ellipse) is intersected by the projection of the companion star at four points (A, B, A' and B'). The straight line AA' and BB' intersect the X axis at point C and point D respectively. The ellipse intersects the X axis at two points C' and D'. The occulted area during maximum eclipse is the area covered by the circular arc AB and A'B' and elliptic arc AA' and BB' (i.e. within AA'B'BA). This area is double the area covered by ABD'C'A. The region filled with hollow circles is the area covered by circular arc AB and straight lines BD, DC and CA. The two regions filled with vertical bars are covered by AC'CA and BDD'B are the regions enclosed by the elliptic arc AB, straight lines C'C, CA and elliptic arc BD', straight lines D'D, DB respectively. The derivation of these areas and finally the visible area are given in section 5.

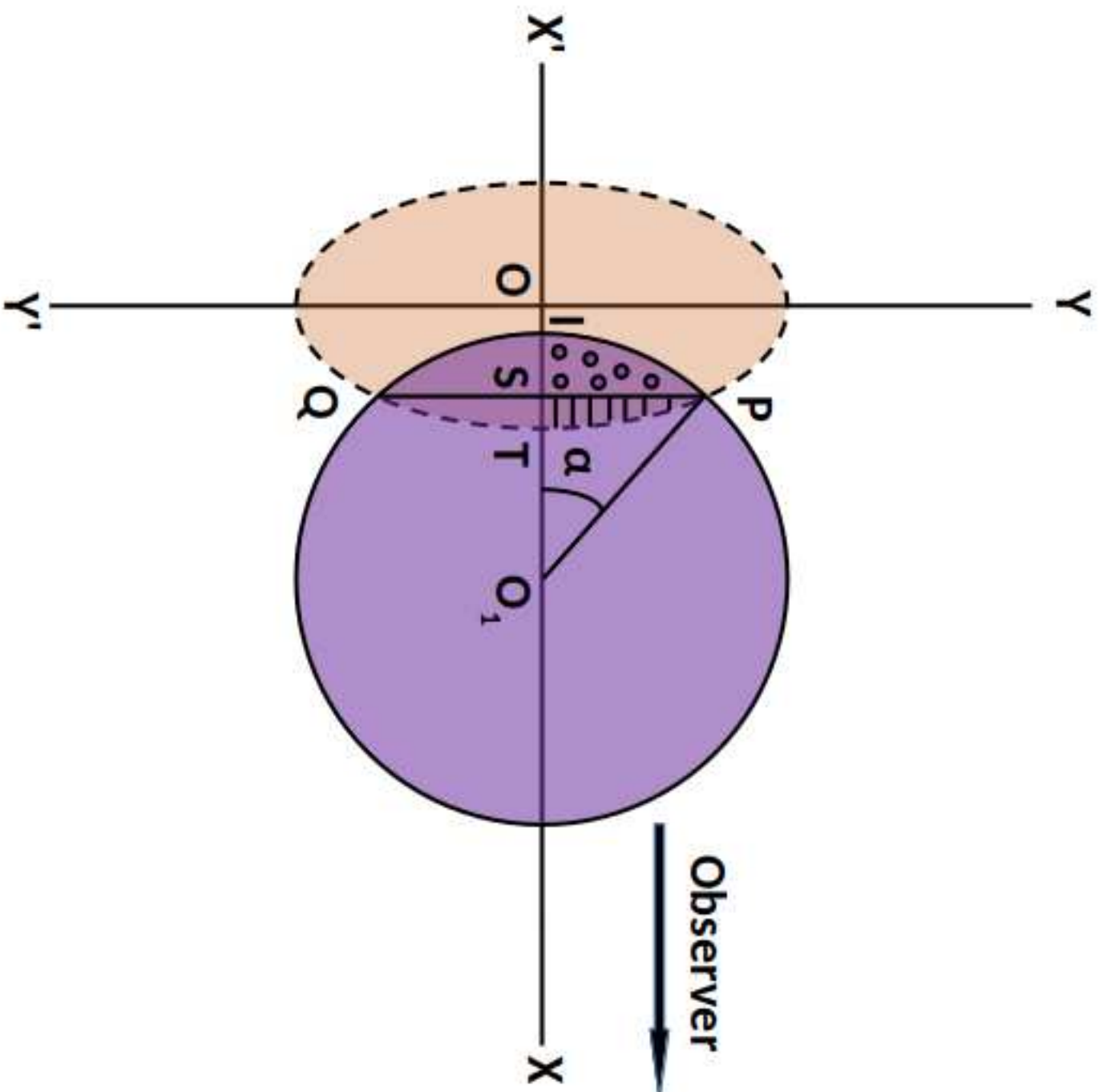
The visible area of the accretion disk =  $A_{\text{visible},4p} = A_{\text{disk}} - A_{\text{occult},4p}$   
 The percentage of the area of the accretion disk visible during total eclipse =  $A_{\text{visible},4p} (\%)$   
 $(A_{\text{visible},4p}/A_{\text{disk}}) \times 100\%$

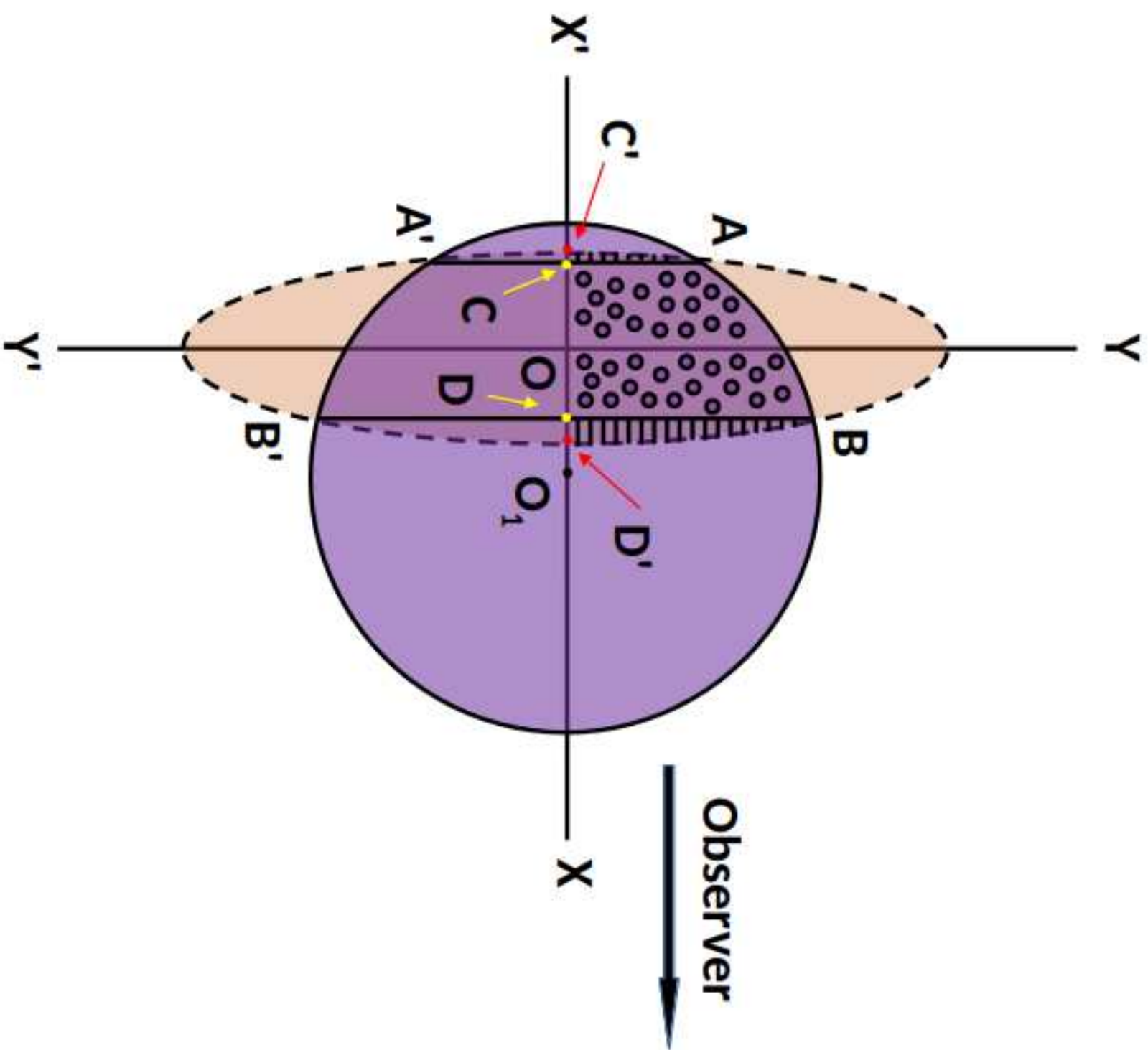
## References

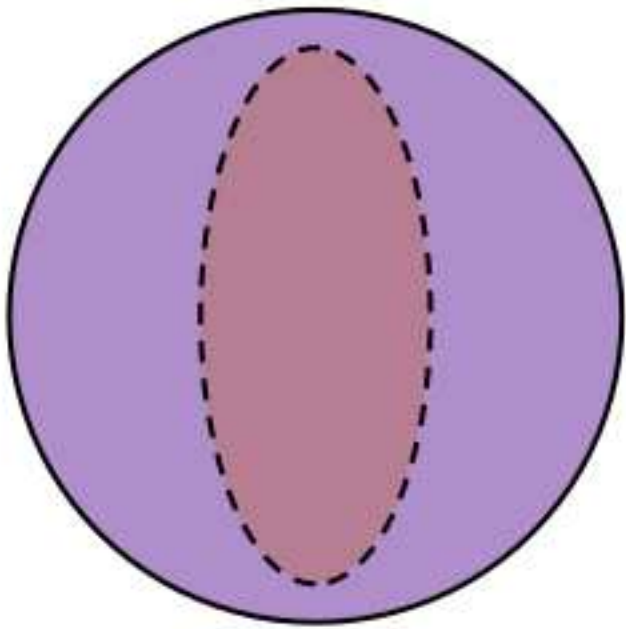
- Aftab N., Paul B., Kretschmar P. X-Ray Reprocessing: Through the Eclipse Spectra of High-mass X-Ray Binaries with *XMM-Newton*. *ApJS* 2019; 243: 29.
- Arnaud, K. A.XSPEC: The First Ten Years. ASP Conf. Series, Vol. 101, Astronomical Data Analysis Software and Systems, ed. G. H. Jacoby & J. Barnes, 17.
- Bland-Hawthorn and Gerhard. The Galaxy in Context: Structural, Kinematic, and Integrated Properties. *Annu. Rev. Astron. Astrophys* 2016; 54: 529-596.
- Boirin L., Keek L., Méndez M., Cumming A., in't Zand J. J. M., Cottam J., Paerels F., Lewin W. H. G. Discovery of X-ray burst triplets in EXO 0748–67. *A&A* 2007; 465: 559-573.
- Cominsky L. R., Wood K. S. Discovery of a 7.1 hour period and eclipses from MXB 1659–29. *ApJ* 1984; 283: 765-773.
- Cominsky L. R., Wood K. S. Further Observations of the Eclipsing X-Ray Burst Source MXB 1659–29. *ApJ* 1989; 337, 485.
- Cottam J., Paerels F., Méndez M., Boirin L., Lewin W. H. G., Kuulkers E., Miller J. M. The Burst Spectra of EXO 0748–676 during a Long 2003 *XMM-Newton* Observation. *ApJ* 2008; 672: 504-509.
- Court et al. 2019. The eclipsing accreting white dwarf Z chameleontis as seen with TESS. *MNRAS*, *MNRAS* 2019, 488, 4149-4160
- de Jong, J. A., van Paradijs, J., & Augusteyn, T. Reprocessing of X rays in low-mass X-ray binaries. *A&A* 1996; 314, 484-490
- Diaz Trigo M. & Boirin L. Accretion disc atmospheres and winds in low-mass X-ray binaries. *Astron. Nachr.* 2016; 337, 368
- Diaz Trigo M., Boirin L., Costantini E., Méndez M., Parmar A. *XMM-Newton* observations of the low-mass X-ray binary EXO 0748–676 in quiescenc. *A&A* 2011; 528, A150.
- Diaz Trigo M., Parmar A. N., Boirin L., Mendez M., Kaastra J. S. Spectral changes during dipping in low-mass X-ray binaries due to highly-ionized absorbers. *A&A* 2006; 445: 179-195.
- Frank, J., King, A. and Lasota J. The light curves of Low Mass X-ray Binaries. *A&A* 1987; 178: 137-142.
- Frank, J., King, A. and Raine, D. Frank, J., King, A. and Raine, D. *Accretion Power in Astrophysics*. Cambridge University Press, Cambridge. 2002.
- Galloway D. K., Muno M. P., Hartman J. M., Psaltis D., Chakrabarty D. Thermonuclear (Type I) X-Ray Bursts Observed by the *Rossini X-Ray Timing Explorer*. *ApJS* 2008; 179: 360-422.
- Genzel R. et al. A study of the gas-star formation relation over cosmic time. *MNRAS* 2010; 407: 2091-2108.
- Gierliński, M., Done, C., & Page, K. Reprocessing of X-rays in the outer accretion disc of the black hole binary XTE J1817–330. *MNRAS* 2009; 392, 1106-1114
- Gillessen S. et al. An Update on Monitoring Stellar Orbits in the Galactic Center. *ApJ* 2017; 837, 30.
- Hynes R. I., Jones E. D. The Quiescent Optical and Infrared Counterpart to EXO 0748–676 = UY Vol. *ApJL* 2009; 697: L14-L17.
- Hyodo Y., Ueda Y., Yuasa T., Maeda Y., Makishima K., Koyama K. Timing and Spectral Study of AXJ1745.6–2901 with *Suzaku*. *PASJ* 2009; 61: S99-S106.
- Iaria R. et al. A possible solution of the puzzling variation of the orbital period of MXB 1659-298. *MNRAS* 2018; 473: 3490-3499.
- Jain C., Paul B. Eclipse timings of the LMXB XTE J1710–281: orbital period glitches. *MNRAS* 2011; 413: 2-6.
- Jain C., Paul B., Sharma R., Jaleel A. Indication of a massive circumbinary planet orbiting the low-mass X-ray binary MXB 1658-298. *MNRAS* 2017; 468: L118-L122.
- Jain C., Sharma R., Paul B. Eclipse Timings of the LMXB XTE J1710-281 : discovery of a third orbital period glitch. *MNRAS* 2022; 517: 2131-2137.
- Jimenez-Garate M. A., Raymond J. C., Liedahl D. A. The Structure and X-Ray Recombination Emission of a Centrally Illuminated Accretion Disk Atmosphere and Corona. *ApJ* 2002; 581: 1297-1327.
- Jin C., Ponti G., Haberl F., Smith R. Probing the interstellar dust towards the Galactic Centre: dust-scattering halo around AX J1745.6–2901. *MNRAS* 2017; 468: 2532-2551.
- Jin C., Ponti G., Haberl F., Smith R., Valencic L. Effects of interstellar dust scattering on the X-ray eclipses of the LMXB AX J1745.6–2901 in the Galactic Centre. *MNRAS* 2018; 477: 3480-3506.
- Knight Amy H., Ingram Adam, Middleton Matthew and Drake Jeremy. Eclipse mapping of EXO 0748-676: evidence for a massive neutron star. *MNRAS* 2022; 510: 4736-4756.

- Kubota A. et al. Evidence for a Black Hole in the X-Ray Transient GRS 1009-45. *PASJ* 1998; 50: 667-673.
- Lewin W. H. G., Hoffman J. A., Doty J., Liller W. X-Ray Bursts. *IAU Circ.* 1976; 2994, 2.
- Liu Q. Z., van Paradijs J., van den Heuvel E. P. J. A catalogue of low-mass X-ray binaries in the Galaxy, LMC, and SMC (Fourth edition). *A&A* 2007; 469: 807-810.
- Lumb D. H., Scharfel N., Jansen F. A. *XMM-Newton* (X-Ray Mult-Mirror Mission) Observatory. *ArXiv e-prints* 2012; 1202.1651.
- Maeda Y., Koyama K., Sakano M., Takeshima T., Yamauchi S. A New Eclipsing X-Ray Burster near the Galactic Center: A Quiescent State of the Old Transient A1742-289. *PASJ* 1996; 48: 417-423.
- Markwardt C. B., Marshall F. E., Swank J., Takeshima T. XTE J1710-281 = 1RXS J171012.3-280754. *IAU Circ.* 1998; 6998, 2.
- Masetti N. et al. IGR J16194-2810: a new symbiotic X-ray binary. *A&A* 2007; 470: 331-337.
- Mason K. O. et al. The *XMM-Newton* optical/UV monitor telescope. *A&A* 2001; 365: L36-L44.
- Mathis, J. S., Rimpl, W. and Nordsieck, K. H. The size distribution of interstellar grains. *ApJ* 1977; 217: 425-433.
- Mitsuda K., Takeshima T., Kii T. Dust-Grain Scattering of X-Rays Observed during the Lunar Occultation of a Transient X-Ray Source near the Galactic Center. *ApJ* 1990; 353, 480.
- Muñoz-Darias T. et al. Dynamical constraints on the neutron star mass in EXO 0748-676. *MNRAS*; 394: L136-L140.
- Nespoli E., Fabregat J., Mennickent R. E. K-band spectroscopy of IGR J16358-4726 and IGR J16393-4643: two new symbiotic X-ray binaries. *A&A* 2010; 516, A94.
- Ozel F, Psaltis D, Narayan R and Santos Villarreal A. On the Mass Distribution and Birth Masses of Neutron Stars. *ApJ* 2012; 757, 55.
- Parmar A. N., Gottwald M., Haberl F., Giommi P., White N. E. Recent Results on Cataclysmic Variables. The Importance of IUE and Exosat Results on Cataclysmic Variables and Low-Mass X-Ray Binaries, Burke W. R., ed. EXO:0748-676 - an Exciting New X-Ray Transient. Recent Results on Cataclysmic Variables. In: Burke W. R., editor. Recent Results on Cataclysmic Variables. The Importance of IUE and Exosat Results on Cataclysmic Variables and Low-Mass X-Ray Binaries, Proceedings of an ESA workshop 1985, 236, 119.
- Parmar A. N., White N. E., Giommi P., Gottwald M. The Discovery of 3.8 Hour Periodic Intensity Dips and Eclipses from the Transient Low-Mass X-Ray Binary EXO 0748-676. *ApJ* 1986; 308, 199.
- Paul B., Archana M., Saripalli L. Simultaneous X-ray and optical observations of thermonuclear bursts in the LMXB EXO 0748-676. *Bulletin of the Astronomical Society of India* 2012; 40: 93-104.
- Ponti, G. et al. Evolution of the disc atmosphere in the X-ray binary MXB 1659-298, during its 2015-17 outburst. *MNRAS* 2019; 487: 858-870.
- Ponti G. et al. *NuSTAR* + *XMM-Newton* monitoring of the neutron star transient AX J1745.6-2901. *MNRAS* 2018; 473: 2304-2323.
- Ponti G., De K., Muñoz-Darias T., Stella L., Nandra K. The puzzling orbital period evolution of the LMXB AX J1745.6-2901. *MNRAS* 2017; 464: 840-849.
- Ponti G. et al. On the Fe K absorption - accretion state connection in the Galactic Centre neutron star X-ray binary AX J1745.6-2901. *MNRAS* 2015; 446: 1536-1550.
- Ponti G., Muñoz-Darias T., Fender R. P. A connection between accretion state and Fe K absorption in an accreting neutron star: black hole-like soft-state winds? *MNRAS* 2014; 444: 1829-1834.
- Psaradaki I., Costantini E., Mehdipour M., Diaz Trigo M. Modelling the disc atmosphere of the low mass X-ray binary EXO 0748-676. *A&A* 2018; 620. A129.
- Raman G., Maitra C., Paul B. Observation of variable pre-eclipse dips and disc winds in the eclipsing LMXB XTE J1710-281. *MNRAS* 2018; 477: 5358-5366.
- Różańska A., Madej J., Bagińska P., Hryniewicz K., & Handzlik B. Disk emission and atmospheric absorption lines in black hole candidate 4U 1630-472. *A&A* 2014; 562, A81.
- Raman G., Paul B. X-ray and optical orbital modulation of EXO 0748-676 : A co-variability study using *XMM-Newton*. *New A* 2017; 54: 122-139.
- Sidoli L., Oosterbroek T., Parmar A. N., Lumb D., Erd C. An *XMM-Newton* study of the X-ray binary MXB 1659-298 and the discovery of narrow X-ray absorption lines. *A&A* 2001; 379: 540-550.
- Smith, R. K., Valencic L. A. and Corrales L. The Impact of Accurate Extinction Measurements for X-Ray Spectral Models. *ApJ* 2016; 818, 143.
- Strüder L. et al. The European Photon Imaging Camera on *XMM-Newton*: The pn-CCD camera. *A&A* 2001; 365: L18-L26.
- Suleimanov, V., Meyer, F., & Meyer-Hofmeister, E. High efficiency of soft X-ray radiation reprocessing in supersoft X-ray sources due to multiple scattering. *A&A* 2003; 401, 1009-1015
- Turner M. J. L. et al. The European Photon Imaging Camera on *XMM-Newton*: The MOS cameras. *A&A* 2001; 365, L27-L35.
- Wijnands R. et al. The Burst Behavior of the Eclipsing Low-Mass X-Ray Binary MXB 1659-298. *ApJ* 2002; 566: 1060-1068.

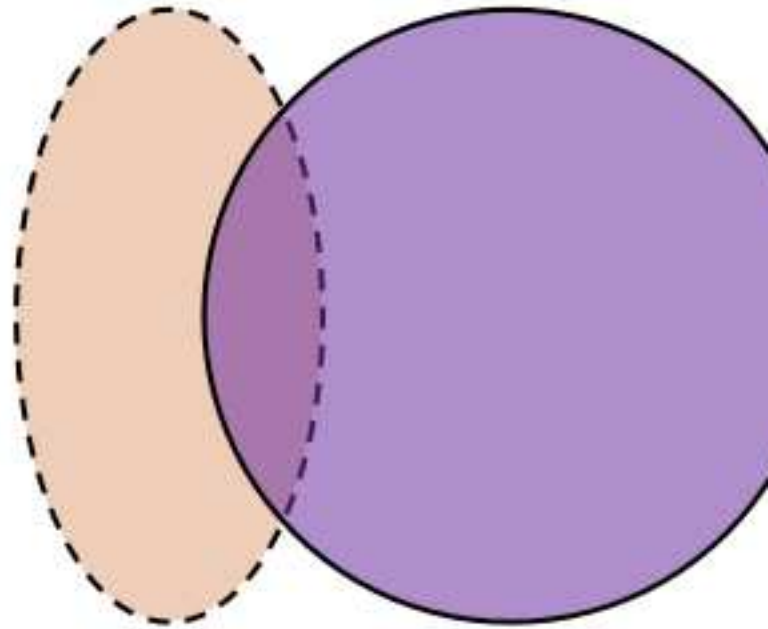
- Wilms, J., Allen, A. and McCray, R. On the Absorption of X-Rays in the Interstellar Medium. *ApJ* 2000; 542: 914-924.
- Wolff M. T. et al. Eclipse timings of the transient Low-Mass X-Ray Binary EXO 0748–676. IV. The Rossi X-ray Timing Explorer Eclipses. *ApJS* 2009; 183: 156-170.
- Wolff M. T. et al. A Strong X-Ray Burst from the Low-Mass X-Ray Binary EXO 0748–676. *ApJ* 2005; 632: 1099-1103.
- Wolff M. T. et al. Eclipse Timings of the Low-Mass X-Ray Binary EXO 0748–676. III. Orbital Period Jitter Observed with the Unconventional Stellar Aspect Experiment and the Rossi X-Ray Timing Explorer. *ApJ* 2002; 575: 384-396, 2002.
- Younes G., Boirin L., Sabra B. An *XMM-Newton* view of the dipping low-mass X-ray binary XTE J1710–281. *A&A* 2009; 1099-1103.
- Zycki P. T., Krolik, J. H., Zdziarski, A. A., & Kallman, T. R. X-Ray Reflection from Photoionized Media in Active Galactic Nuclei. *ApJ* 1994; 437, 597







**(i)**



**(ii)**